scientific reports

Check for updates

OPEN

Mechanistic insights into the P-coumaric acid protection against bisphenol A-induced hepatotoxicity in in vivo and in silico models

Samet Tekin[1]✉, Merve Bolat[1], Aslıhan Atasever[1], İsmail Bolat[2], Burak Çinar[3], Azizeh Shadidizaji[4], Yusuf Dağ[1], Emin Şengül[1], Serkan Yildirim[2], Ahmet Hacimuftuoglu[3] & Mohamad Warda[1,5]

Bisphenol A (BPA), commonly found in plastic containers and epoxy resins used for food products, presents substantial health risks, particularly in relation to hepatic toxicity. This study investigates BPA-induced liver damage and explores the mechanistic dose-dependent protective effects of P-coumaric acid (PCA). 50 male rats were divided into control, BPA-treated, BPA + PCA50, BPA + PCA100, and PCA100 groups. BPA exposure for 14 days induced oxidative stress, evidenced by elevated malondialdehyde levels and decreased activities of antioxidant enzymes (superoxide dismutase, glutathione peroxidase, and catalase). Higher doses of PCA effectively mitigated these effects by restoring redox balance and enhancing antioxidant enzyme activities. Additionally, BPA disrupted inflammation and apoptosis pathways, inhibiting anti-inflammatory markers and interfering with the nuclear factor erythroid 2-related factor 2/heme oxygenase-1 (Nrf2/HO-1) pathway. PCA exhibited dose-dependent protection against these disruptions. Computational analyses revealed that BPA inhibits cyclooxygenase-1 through stable hydrogen bonding with threonine at position 322. PCA's dual protective effect was confirmed by attenuating inflammatory pathways, including TNF-α inhibition and suppression of the Kelch-like ECH-associated protein 1 (KEAP1) and Nrf2 signaling pathway. Histopathological assessments confirmed that PCA alleviated significant hepatic damage induced by BPA. Immunohistochemical and immunofluorescence analyses further supported PCA's protective role against BPA-induced apoptosis and cellular hepatotoxicity. These findings underscore PCA's protective potential against BPA-induced hepatotoxicity and highlight novel mechanistic interactions that warrant further investigation in applied nutritional biochemistry.

Keywords Apoptosis, Bisphenol A, In silico, Inflammation, Oxidative stress, P-Coumaric acid

BPA is a synthetic chemical compound extensively employed in the production of polycarbonate plastics and epoxy resins. It is synthesized through the condensation of two phenol molecules and one acetone molecule in the presence of concentrated sulfuric acid[1]. BPA is prevalent in the manufacturing of numerous consumer products, including plastic containers, food and beverage packaging, dental sealants, and the lining of metal cans, as well as in baby milk and mineral water containers[2,3]. BPA can leach from these products and enter the food or beverages that they contain. Recent global studies have shown that BPA is widely detected in various environmental matrices and biological samples, highlighting the significant extent of human and ecological exposure. BPA has been frequently identified in water sources, such as rivers, lakes, and groundwater, often at concentrations ranging from nanograms to micrograms per liter, depending on the proximity to industrial or urban sources[4]. The compound has been found to persist in the environment its slow degradation rate, leading to ongoing contamination of aquatic ecosystems. Furthermore, BPA contamination has been detected in sediments and soils, further indicating its widespread environmental presence[5]. In biological contexts, BPA has been detected in human tissues, including urine, blood, and breast milk, with studies showing detectable

[1]Department of Physiology, Faculty of Veterinary Medicine, Atatürk University, Erzurum, Turkey. [2]Department of Pathology, Faculty of Veterinary Medicine, Atatürk University, Erzurum, Turkey. [3]Department of Medical Pharmacology, Faculty of Medicine, Atatürk University, Erzurum, Turkey. [4]Department of Plant Biotechnology, Faculty of Agriculture, Ataturk University, Erzurum, Turkey. [5]Department of Biochemistry, Faculty of Veterinary Medicine, Cairo University, Giza, Egypt. ✉email: samet.tekin@atauni.edu.tr

levels in a substantial proportion of the population across various age groups and regions[5]. For instance, BPA concentrations in human urine often exceed levels considered to pose potential health risks, even with regulatory measures in place. Additionally, wildlife studies have revealed the presence of BPA in various species, ranging from fish to invertebrates, underscoring its bioaccumulative properties and its potential to affect ecological balance and biodiversity[6]. These detection levels reflect the ongoing concern about the ubiquity of BPA and its potential adverse effects on human health, particularly its role as an endocrine disruptor affecting reproductive, metabolic, and neurological functions[4,7].

Upon oral ingestion, BPA is absorbed from the gastrointestinal tract and undergoes conjugation to form BPA glucuronide in the liver. This absorption occurs when individuals consume contaminated food or water[8]. BPA then accumulates in the enterohepatic circulation over time in the bloodstream[9]. Consequently, elevated levels of BPA result in its binding to estrogen receptors, triggering adverse cellular responses[10,11] and inducing both cellular and toxic effects in reproductive organs[12,13]. Recent studies have shown that it can cause extensive damage to other organs[14–16]. The induction of hepatotoxic effects is characterized by increased activity of hepatic enzymes and an increased state of oxidative stress, coupled with a concomitant increase in reactive oxygen species (ROS) levels. This perturbation manifests as a deviation in hepatic redox balance toward oxidative stress, accompanied by diminished antioxidant reserve and reduced levels of antioxidant enzymes within the hepatic milieu. Simultaneously, there is an increase in hepatic oxidants. This disruption in cellular redox homeostasis subsequently initiates inflammatory responses within hepatic cells, stimulating oxidative stress and concurrently intensifying the activation of the cellular Nrf2/HO-1 pathway[16–19]. The application of BPA further exacerbates the depletion of cellular anti-inflammatory reserves, accompanied by a simultaneous increase in proinflammatory mediators[20]. Prolonged exposure to these conditions directs the cell toward apoptosis[21,22].

Conversely, among the various plant-derived nutraceutical compounds explored for their protective effects against diverse toxic substances, P-coumaric acid (PCA) stands out. PCA, belonging to the hydroxycinnamic family, is naturally present in various fruits, vegetables, and fungi[23,24]. Numerous studies have demonstrated the antioxidant, anti-inflammatory, and antiapoptotic effects of PCA[25,26]. In this context, PCA has emerged as a promising nutraceutical countermeasure against the disruptive effects of factors such as BPA, providing protection against oxidative stress, inflammation, and apoptotic pathways in hepatic cells.

This study aimed to evaluate the hepatoprotective efficacy of PCA against BPA-induced oxidative stress and subsequent hepatic insult in a rat model. The biomolecular intricacies governing the ameliorative effects of PCA were investigated, emphasizing its role in mitigating BPA-induced oxidative stress, inflammation, and subsequent apoptotic liver damage. To comprehensively understand the molecular mechanisms of PCA, an in silico study was conducted, revealing its inhibitory effects on oxidative stress and proinflammatory upstream modulators. Additionally, a computational approach was employed to elucidate the recognized inhibitory impact of BPA on COX1 enzyme activity. The investigation of potential ligand–ligand interactions between BPA and PCA confirmed the biochemical contribution of PCA to alleviating BPA-induced hepatic injury. This research provides novel insights into the protective mechanisms of PCA and reveals its intricate biochemical interaction with BPA, establishing a foundation for addressing and modulating chemical-induced liver damage.

Methods

Chemicals

BPA (≥99%) (Cas No: 80-05-7) and PCA (≥98%) (Cas No: 501-98-4) were purchased from Acros Organics BVBA and Sigma-Aldrich Chemical Company (St. Louis, Missouri, USA), respectively. ELISA kits were purchased from BT LAB.

Animals and experimental design

Fifty healthy 14-week-old male adult rats were procured from the Atatürk University Experimental Animals Application and Research Centre. The weights of all the rats were measured both at the beginning and at the end of the experiment. The experimental animals were randomly divided into 5 groups, each comprising 10 animals[27]. The baseline weights of the rats in all five groups were statistically analyzed, revealing no significant differences among groups ($p > 0.05$), confirming uniform baseline conditions prior to the experiment. A computer-generated random number algorithm was employed to randomly assign animals into the five experimental groups, ensuring the elimination of allocation bias. Prior to the experiment, the environment and cages were cleaned and disinfected, which was completed 7 days in advance. Four days before the initiation of the experiment, the rats were acclimatized to the environment by being housed in the designated rooms. This was followed by an experimental period of 14 days, during which the animals were housed in rooms maintained at 25 °C 60 ± 10% humidity, and a 12-h light/dark cycle. Temperature and humidity were continuously monitored using calibrated digital sensors, with daily data recording to ensure stable conditions throughout the study. There were no restrictions on the animals' access to water or food. Approval for this study was obtained from the Atatürk University Animal Experiments Local Ethics Committee. (Decision No: 2023/87). The study is reported in accordance with the ARRIVE guidelines. Moreover, all methods were performed in accordance with the relevant guidelines and regulations required by the Atatürk University Animal Experiments Local Ethics Committee.

BPA and PCA were administered to rats in 5 experimental groups, each consisting of 10 animals. The groups were designated the control, BPA, BPA + PCA50, BPA + PCA100, and PCA100 groups. All the groups were treated for 14 days[28,29]. The rats in the control group were subjected to intragastric administration of 1 ml of olive oil. The BPA groups received a 100 mg/kg dose of BPA dissolved in olive oil through intragastric administration.

Olive oil was selected as a vehicle control due to its widespread use in toxicity and pharmacological studies as an inert solvent for lipophilic compounds, with minimal biological activity, making it a suitable comparator for assessing the effects of BPA and PCA. The PCA groups were intragastrically administered 50 or 100 mg/kg

PCA for 14 days[28,29]. On the 15th day of the experimental period, the animals were weighed before euthanasia. After the animals were euthanized with sevoflurane, a portion of the liver tissue was fixed with formaldehyde for histopathological, immunohistochemical, and immunofluorescent analyses[30]. Concurrently, the remaining liver tissues were rapidly frozen in liquid nitrogen and stored at −80 °C. These preserved samples were used for subsequent assessments of oxidative stress, inflammation, and apoptotic parameters. After the results were calculated through the GEN5 program, statistical analyses were performed. GraphPad Prism 8 was used to create the graphs[13].

Hepatic tissue homogenization

The liver tissues were homogenized in PBS using a MagNA Lyser at 6000 rpm for 40 s. A volume of 1 mL of PBS per 100 mg of liver tissue was used. After homogenization, the supernatants were recovered via centrifugation at 4500 rpm for 10 min at 4 °C. The recovered supernatants were further subjected to ELISA[13].

Oxidative stress and antioxidant evaluation in liver tissue

The hepatic oxidative stress status was evaluated by measuring the activities of antioxidant enzymes, including superoxide dismutase (SOD) (Cat. No: E0168Ra), glutathione peroxidase (GPx) (Cat. No: E1242Ra), catalase (CAT) (Cat. No: E0869Ra), and glutathione synthetase (GSS) (Cat. No: E1989Ra), as well as the hepatic level of the lipid peroxidation marker malondialdehyde (MDA) (Cat. No: 201-11-0157) (Zhejiang, China) in the recovered supernatants. All these assessments, together with measurements of the levels of nuclear factor erythroid 2-related factor 2 (Nrf-2) (Cat. No: E2184Ra) and heme oxygenase 1 (HO-1) (Cat. No: E0676Ra), which are hepatic antioxidant detoxifying parameters (Zhejiang, China), were conducted via ELISA kits.

Inflammation in liver tissue

The levels of proinflammatory mediators such as tumor necrosis factor-α (TNF-α) (Cat. No: E0764Ra), interleukin-1β (IL-1β) (Cat. No: E0119Ra), interleukin-6 (IL-6) (Cat. No: E0135Ra), nuclear factor kappa-B (NF-κB) (Cat. No: E1817Ra), and other anti-inflammatory cytokine interleukin-10 (IL-10) (Cat. No: E0108Ra) were determined via ELISA (Zhejiang, China).

The levels of other inflammatory mediators, including myeloperoxidase (MPO) (Cat. No: E0574Ra), inducible nitric oxide synthase (iNOS) (Cat. No: E0740Ra), prostaglandin E2 (PGE2) (Cat. No: EA0039Ra) and cyclooxygenase-1 (COX-1) (Cat. No: E1245Ra), were determined by ELISA in hepatic tissues (Zhejiang, China).

Apoptosis in liver tissue

Caspase-3 (Casp-3) (Cat. No: E1668Ra) and p38 mitogen-activated protein kinase (p38-MAPK) (Cat. No: E2473Ra) levels were determined to determine whether apoptosis occurred in liver tissue (Zhejiang, China).

In silico molecular elucidation of BPA-induced inhibition of COX-1 (PDB: 3N8Z) activity

Ligands and protein preparation

The observed biological inhibition of COX-1 activity by BPA prompted a more in-depth investigation into the molecular basis of this inhibition at the COX-1 active site via in silico analysis. Therefore, the 3D structure of BPA (PubChem CID 6623) was obtained from the PubChem database[31], and the minimization and optimization of CID 6623 of BPA were then performed via ChemBioDraw Ultra 14 suite software[32]. The X-ray crystal coordinates of COX-1 (PDB: 3N8Z) were then retrieved from the RCSB Database[33], followed by the creation of PDBQT files for both receptors and ligands via UCSF Chimera software 1.17.3[34]. Subsequently, preparation for docking was carried out via the Dunbrack 2010 rotamer library[35]. Additionally, minimization of the receptor structure (Steepest descent steps: 100; Conjugate gradient step: 10) was performed via UCSF Chimera 1.17.3 software (Fig. 9).

Molecular docking protocol

The active site of the COX-1 protein was obtained from an online server[36]. Second, the grid box size was fixed at 20 × 20 × 20 Å, and the grid center (−54,186; 54,440; −0.826) for the COX-1 enzyme active site was set according to the setting software. Molecular docking of BPA and COX-1 was performed with UCSFChimera + Autodockvina32 software[37]. PyMOL software was utilized to generate a 3D representation of the BPA and COX-1 complex in the study[38].

BPA-COX-1 complex interaction

The Protein Ligand Interaction Profiler (PLIP) server was used[39]. The 2D BPA-COX-1 complex was obtained from Discovery Studio Visualizer v21.1.0.20298[40].

Interaction between bisphenol A and p-coumaric acid

The observed quenching effect of PCA against BPA-induced hepatotoxicity inspired us to conduct an in silico investigation into potential collateral ligand–ligand chemical interactions. This possible chemical interaction could explain the biological mitigating effect of PCA against BPA-induced hepatic toxicity. Therefore, the following studies were performed.

Molecular models and initial structures

The chemical structures of the compounds were obtained from the PubChem server (PubChem CID: BPA = 6623 and PCA = 637542)[41] (Fig. 9B,D). The monomer molecules were fully optimized at the M062X/6-311G** level of theory via Gaussian 09 software[42].

Molecular mechanics calculations

For molecular mechanics calculations, the initial structures were subjected to optimization via Gaussian 09 software. This step provided a foundation for subsequent quantum mechanical calculations[43].

Quantum mechanical calculations

The quantum mechanical (QM) calculations were carried out on the extracted BPA–PCA complexes obtained from molecular mechanics calculations via Gaussian 09. The global hybrid meta-GGA (M06-2X) functional group was employed to optimize these complexes. This functional is known for its accurate simulation of hydrogen bonds and proficient representation of other weak interactions.

The optimization process utilized the 6-31G** Gaussian basis set, incorporating polarized functions for both heavier and hydrogen atoms[43]. To ensure the reliability of the optimized structures, normal vibrational frequencies were computed through single-point calculations. The confirmation of minima on the potential energy surface was established by verifying positive values for the Hessian eigenvalues.

This comprehensive methodology aimed to capture the intricacies of molecular interactions, particularly focusing on the accurate representation of hydrogen bonds and other subtle weak interactions within the BPA–PCA complexes (Fig. 12).

In silico molecular assessment of the modulatory potential of PCA on the KEAP1-Nrf2 pathway and TNF trimer stability

The exploration of the antioxidative effects of PCA prompted our biological study to assess the potential impact of PCA on the KEAP1-Nrf2 pathway and the stability of the TNF trimer. Keap1, a cytoplasmic protein, acts as a negative upstream modulator of Nrf2, making this pathway a promising therapeutic target for mitigating oxidative damage caused by free radicals. Conversely, TNF, a cytokine within the trimeric protein family, plays a crucial role in various pathological processes, particularly inflammation initiation and apoptosis. The downregulation of TNF is acknowledged for its anti-inflammatory effects, which are achieved by suppressing the signaling pathways associated with TNF and subsequently reducing the production of proinflammatory molecules. Therefore, we systematically examined the inhibitory potential of PCA on the KEAP1–Nrf2 pathway and TNF trimer stability through the following in silico methodologies to determine its potential modulatory role in these pivotal processes.

Molecular structures of KEAP1, TNF trimers and PCA

The 3D SDF file of PCA was downloaded from https://pubchem.ncbi.nlm.nih.gov/. The molecular structures of KEAP1 and TNF trimers (PDB codes: 6LRZ and 6OOY) were downloaded from the Protein Data Bank (PDB), and preparations were made via the licensed version of Schrödinger Maestro 2023/4.

Molecular docking of PCA with KEAP1 and TNF trimers

Molecular docking was performed via the Glide module to predict ligand–receptor interactions. Molecular docking of PCA onto these two protein structures was performed via the licensed version of Schrödinger Maestro 2023/4[44].

Surface, 2D and 3D visualization

To better understand the molecular interactions, images were downloaded via Schrödinger Maestro's surface and 2D and 3D imaging tools. This allowed interaction sites to be visualized[45].

MM-GBSA analysis

MM-GBSA was performed via the Prime MM-GBSA module. This analysis includes interaction energies, solvation energies and other thermodynamic properties[46].

Pharmacophore mapping analysis

The ligand pharmacophore mapping feature of Glide was used to identify the interaction sites between ligands and receptors. The important interaction motifs were identified by generating pharmacophore maps[47].

Molecular dynamics analysis

Molecular dynamics simulations were performed via the Desmond module. This was done to understand the changes in the interactions over time and the dynamic behavior of the protein[48].

All of these in silico analyses were performed using the 2023/4 licensed version of Schrödinger Maestro.

Histopathological examination

The liver tissue samples were fixed in a 10% formaldehyde solution for 48 h and subsequently embedded in paraffin blocks following routine tissue processing procedures. Sections, each measuring 4 µm in thickness, were obtained from the blocks, and the resulting preparations for histopathological examination were stained with hematoxylin–eosin (HE). A light microscope (Olympus BX 51, Japan) was used to examine the stained sections, and their histopathological features were evaluated and categorized as absent (–), mild (+), moderate (++), or severe (+++).

Immunohistochemical examination

For immunoperoxidase examination, tissue sections taken on adhesive (poly-L-lysine) slides were deparaffinized and dehydrated. The endogenous peroxidase was then inactivated with 3% H_2O_2 for 10 min. The tissues were boiled in 1% antigen retrieval citrate buffer solution (pH 6.1). After cooling at room temperature, the sections

were incubated with protein blocks for 5 min to abolish nonspecific background staining. The primary antibody (Bax Cat No: sc-7480, dilution ratio: 1/100, US) was then added prior to further incubation according to the manufacturer's instructions. The 3–3′ diaminobenzidine (DAB) chromogen was used as the tissue chromogen. The stained sections were then examined with a light microscope (Zeiss AXIO, Germany).

Double immunofluorescence examination

For immunoperoxidase examination, tissue sections affixed to adhesive (poly-L-lysine) slides were subjected to deparaffinization and dehydration. The endogenous peroxidase activity was subsequently neutralized by immersing the sections in 3% H_2O_2 for 10 min. The tissues were then boiled in a 1% antigen retrieval citrate buffer solution at pH 6.1, followed by cooling at room temperature. To mitigate nonspecific background staining, the sections were blocked with protein for 5 min. Then, primary antibody (JNK Cat No: sc-514539, dilution ratio: 1/100, US) was applied, and the samples were incubated as per the provided instructions. The secondary antibody for immunofluorescence (FITC Cat No: ab6785, dilution ratio: 1/1000) was applied to the tissues, which were then incubated in a dark environment for 45 min. The secondary antibody (PERK Cat No: sc-377400, dilution ratio: 1/100, US) was subsequently added to the tissues, which were subsequently incubated according to the provided instructions. Another immunofluorescence secondary antibody (Texas Red Cat No: ab6719, dilution ratio: 1/1000, UK) was applied, and the samples were incubated in the dark for 45 min. Then, DAPI with mounting medium (Cat no: D1306, dilution ratio: 1/200, UK) was added to the sections, which were then left in the dark for 5 min before being covered with a coverslip. The stained sections were examined via a fluorescence microscope (Zeiss AXIO, Germany). For the quantification of positive staining intensity in both the immunohistochemical and the immunofluorescence images, a systematic approach was employed. Specifically, five random regions were selected from each image, and analysis was conducted via the ZEISS Zen Imaging Software program.

Statistical analysis

The data we obtained are presented as the mean ± standard mean error (SEM). The significance level was determined as $p < 0.05$. One-way analysis of variance (ANOVA) was used to determine the differences between groups. SPSS and GraphPad were used for these tests.

SPSS 13.0 was used for the statistical analysis of the histopathological data, and the data were evaluated, with $p < 0.05$ considered to indicate statistical significance. Duncan's test was used for comparisons between groups. The nonparametric Kruskal–Wallis test was used to detect group interactions, and the Mann–Whitney *U* test was used to determine differences between groups.

The acquired immunohistochemical and immunofluorescence data were subjected to additional statistical analysis through the computation of the mean and standard deviation (mean ± SD), specifically emphasizing the percentage area of positive staining. One-way ANOVA followed by Tukey's test, conducted via GraphPad Prism, was subsequently employed to compare the positive immunoreactive cells and immunopositive stained areas with those from healthy controls. Significance was determined by considering a p value less than 0.001.

Results

Impact of BPA and PCA administration on body weight and hepatic mass

At the onset of the study, the weights of all the rats were recorded. Following the grouping, initial body weights, as presented in Table 1, were compared, revealing no statistically significant differences between the groups ($p > 0.05$). At the conclusion of the experiment, body weights were measured once more, and again, no significant differences were observed ($p > 0.05$). Liver weights and the hepatosomatic index (HSI) were comparable among the groups, with no statistically significant differences detected ($p > 0.05$, Table 1).

Assessment of oxidative stress and antioxidant status in hepatic tissues

The MDA level in the liver tissue of BPA-treated rats was significantly greater than that in the control group ($p < 0.01$). The MDA content in the BPA + PCA50 group was lower than that in the BPA group, but a significant difference was observed compared with that in the control group ($p < 0.01$). Notably, the MDA levels in the BPA + PCA100 and PCA100 groups were comparable to those in the control group, with no significant difference between them ($p > 0.05$, Fig. 1).

Oxidative stress was confirmed by the notable decrease in SOD activity in the livers of BPA-treated rats compared with those of control rats ($p < 0.01$). The addition of PCA to BPA, particularly at high doses, effectively

Parameters	Control	Groups			
		BPA	BPA + PCA50	BPA + PCA100	PCA100
Initial body weights (g)	246.43 ± 5.56[a]	245.00 ± 5.00[a]	247.86 ± 4.88[a]	247.86 ± 4.88[a]	244.29 ± 6.07[a]
Final body weights (g)	280.57 ± 28.18[a]	273.57 ± 17.96[a]	274.86 ± 12.32[a]	274.86 ± 12.32[a]	293.14 ± 30.71[a]
Liver weights (mg)	285 ± 10.3[a]	267 ± 10.3[a]	270 ± 10.3[a]	272 ± 10.3[a]	282 ± 10.3[a]
Hepatosomatic Index (HSI)*	0.00100	0.00097	0.00098	0.00099	0.00096

Table 1. Effects of BPA and PCA on the initial, final and liver weights of the rats. No statistical significance was found between the values in the same line. [a]$p > 0.05$, Values were expressed as the mean ± SEM. *The hepatosomatic index represents the perventage ratio between fresh liver weight to whole body weight.

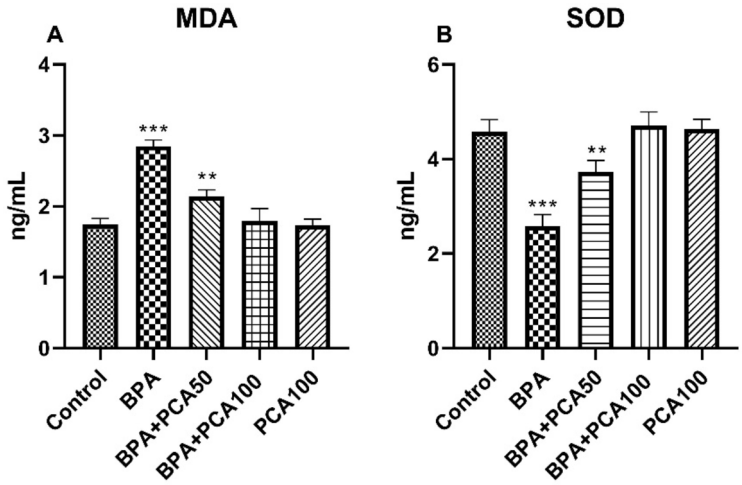

Fig. 1. The effects of BPA and PCA on the MDA (**A**) and SOD (**B**) levels in the experimental groups (significant differences between the control group and the other groups are shown with symbols). ***, $^{**}p < 0.01$, $^{*}p < 0.05$, $n = 10$.

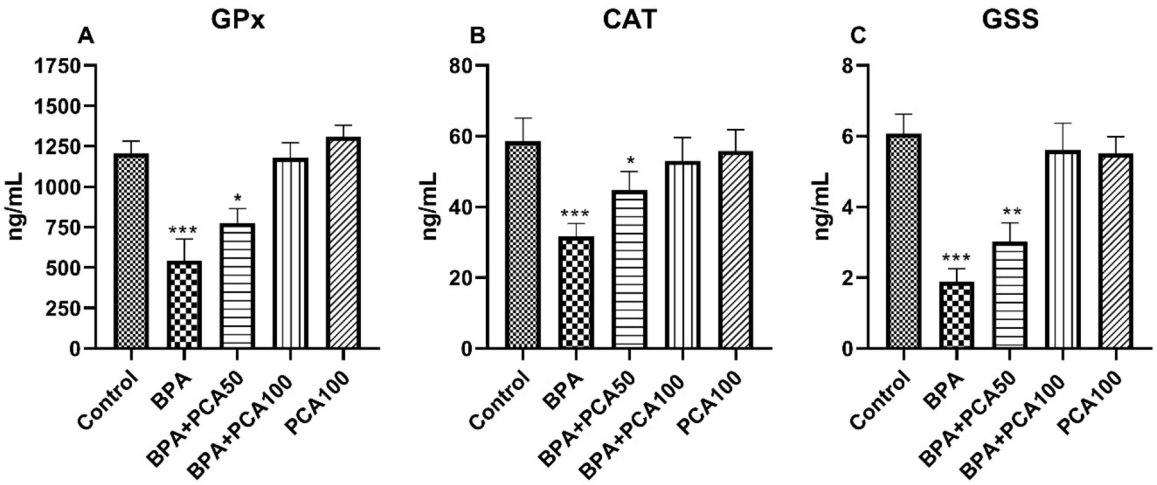

Fig. 2. The effects of BPA and PCA on GPx (**A**), CAT (**B**) and GSS (**C**) levels in the experimental groups (significant differences between the control group and the other groups are shown with symbols). ***, $^{**}p < 0.01$, $^{*}p < 0.05$, $n = 10$.

reversed the decrease in SOD activity observed in the BPA group. However, the SOD level in the BPA + PCA group did not significantly differ from that in the control group ($p > 0.05$, Fig. 1).

Similarly, in BPA-induced liver damage, the activity levels of GPx, CAT, and GSS were significantly lower in the BPA-treated group than in the control group. Compared with those in the BPA + PCA50 group, both GPx and CAT levels in the BPA + PCA50 group increased, but there was still a significant difference compared with those in the control group ($p < 0.05$). The activity of GSS in the BPA + PCA50 group significantly differed from that in the control group ($p < 0.01$). When the values obtained from the BPA + PCA100 and PCA100 groups were compared with those of the control group, no significant difference was observed ($p > 0.05$, Fig. 2).

BPA administration clearly disrupted the cellular redox balance and anti-inflammatory mechanisms, as indicated by a substantial reduction in the levels of Nrf-2 and HO-1 in the livers of the rats treated with BPA compared with those in the control group ($p < 0.01$).

In the BPA + PCA50-treated group, these values were significantly lower ($p < 0.01$) than those in the control group. However, the BPA + PCA100 and PCA100 groups presented no significant differences compared with the control group ($p > 0.05$, Fig. 3).

Assessment of inflammation in BPA-induced hepatotoxicity

BPA-induced inflammation was confirmed by a significant increase ($p < 0.01$) in the levels of the proinflammatory cytokines TNF-α, IL-1β, and IL-6 during BPA-induced liver damage. In the BPA + PCA50 group, there was a slight decrease in these levels, and although this decrease was marginal, a significant difference from the control

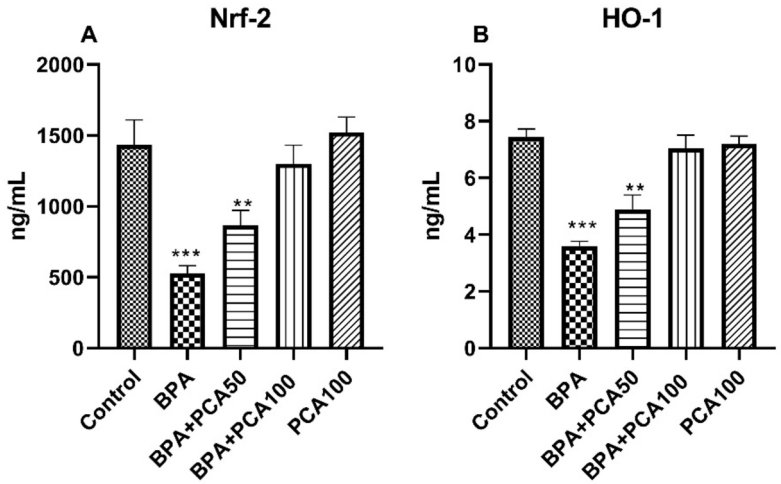

Fig. 3. Effects of BPA and PCA on Nrf-2 (**A**) and HO-1 (**B**) levels in the experimental groups (significant differences between the control group and the other groups are shown with symbols). ***, $^{**}p < 0.01$, $^{*}p < 0.05$, $n = 10$.

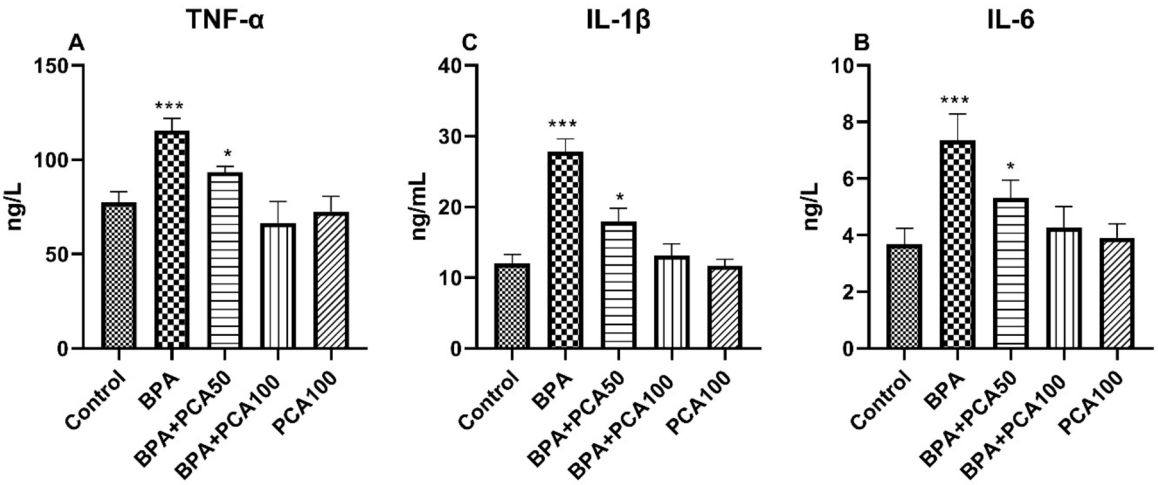

Fig. 4. Effects of BPA and PCA on TNF-α (**A**), IL-1β (**B**) and IL-6 (**C**) levels in the experimental groups (significant differences between the control group and the other groups are shown with symbols). ***, $^{**}p < 0.01$, $^{*}p < 0.05$, $n = 10$.

was maintained ($p < 0.05$). Notably, the TNF-α, IL-1β, and IL-6 levels in both the BPA + PCA100 and PCA groups closely resembled those in the control group ($p > 0.05$, as depicted in Fig. 4).

In contrast, the anti-inflammatory cytokine IL-10 significantly decreased ($p < 0.01$) in the BPA-treated group. In the BPA + PCA50 group, the values closely resembled those of the BPA group, with no significant difference between them ($p > 0.05$). A comparison of values from the BPA + PCA100 and PCA100 groups to the control revealed no significant difference between these groups ($p > 0.05$, as illustrated in Fig. 5).

Consistent with these findings, the level of NF-κB, an inflammatory marker, was significantly greater in the BPA-treated group than in the control group ($p < 0.01$). When the values obtained from the BPA + PCA50 group were compared with those of the control group, a significant difference was observed ($p < 0.01$). There was no significant difference between the BPA + PCA100 and PCA100 groups and the control group ($p > 0.05$, Fig. 5).

PGE2 and COX-1 levels in the liver tissue of BPA-treated rats were significantly lower ($p < 0.01$) than those in the control group. However, the comparison of their values in the BPA + PCA50 group with those in the control group revealed a significant difference ($p < 0.05$). There was no significant difference between their values in the BPA + PCA100 and PCA100 groups compared with those in the control group ($p > 0.05$, as depicted in Fig. 6).

The levels of both the inflammatory mediators iNOS and MPO were notably greater ($p < 0.01$) in the liver tissues of BPA-treated rats than in those of control rats. This significant difference persisted in the BPA + PCA50-treated rats compared with the control rats ($p < 0.01$). However, when the values obtained from the BPA + PCA100 and PCA100 groups were compared with those of the control group, no significant difference was detected

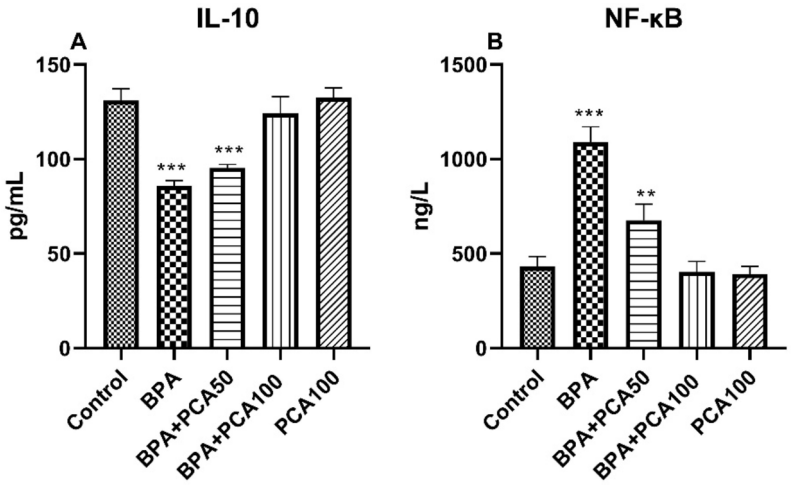

Fig. 5. Effects of BPA and PCA on IL-10 (**A**) and NF-κB (**B**) levels in the experimental groups (significant differences between the control group and the other groups are shown with symbols). ***, **$p < 0.01$, *$p < 0.05$, $n = 10$.

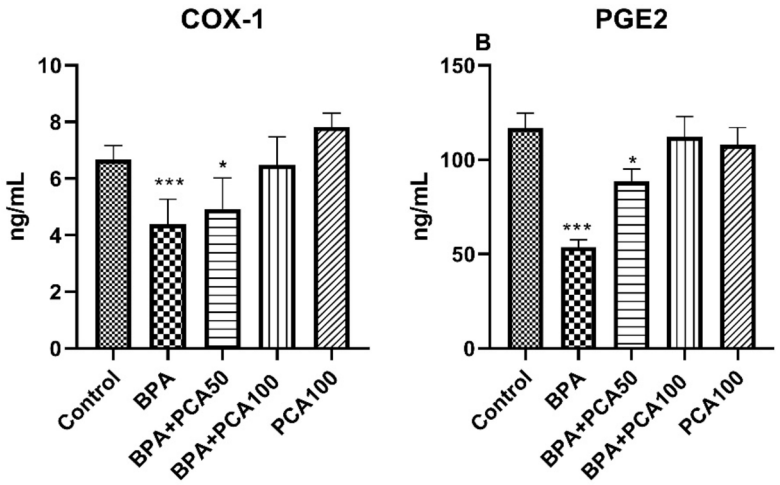

Fig. 6. The effects of BPA and PCA on COX-1 (**A**) and PGE2 (**B**) levels in the experimental groups (significant differences between the control group and the other groups are shown with symbols). ***, **$p < 0.01$, *$p < 0.05$, $n = 10$)

($p > 0.05$, as illustrated in Fig. 7). This finding indicates a notable impact of BPA on the inflammatory milieu, which is partially mitigated by PCA administration.

Molecular mechanisms of apoptosis in BPA-induced hepatic injury

To gain deeper insight into the molecular mechanisms underlying BPA-induced apoptosis, an examination of apoptotic parameters, including Casp-3 and p38-MAPK, revealed a notable increase in their levels in the livers of BPA-treated rats compared with those in the control group ($p < 0.01$). Specifically, the Casp-3 level in the BPA + PCA50-treated group was significantly different from that in the control group ($p < 0.01$). However, no significant differences in p38-MAPK levels were detected between the BPA + PCA50, BPA + PCA100, and PCA100 groups and the control group ($p > 0.05$, Fig. 8).

Docking results

Molecular docking simulation

The binding affinities of BPA for the COX-1 active site

This investigation focused on evaluating the active site of COX-1 through an active site prediction server, revealing the cavity sequence KLDPTFRCWGQEYNVHASIM. Importantly, a molecular docking study revealed that BPA establishes a hydrogen bond with the amino acid threonine (THR) at position 322 of the B chain (subunit) of COX-1 (Fig. 9). The distance between the hydrogen bond donor (BPA) and acceptor (THR 322. B)

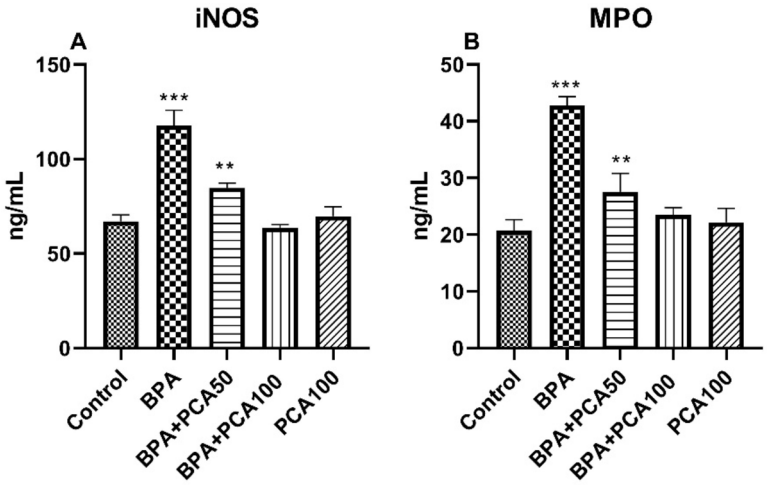

Fig. 7. The effects of BPA and PCA on iNOS (**A**) and MPO (**B**) levels in the experimental groups (significant differences between the control group and the other groups are shown with symbols). ***, $^{**}p < 0.01$, $^{*}p < 0.05$, $n = 10$.

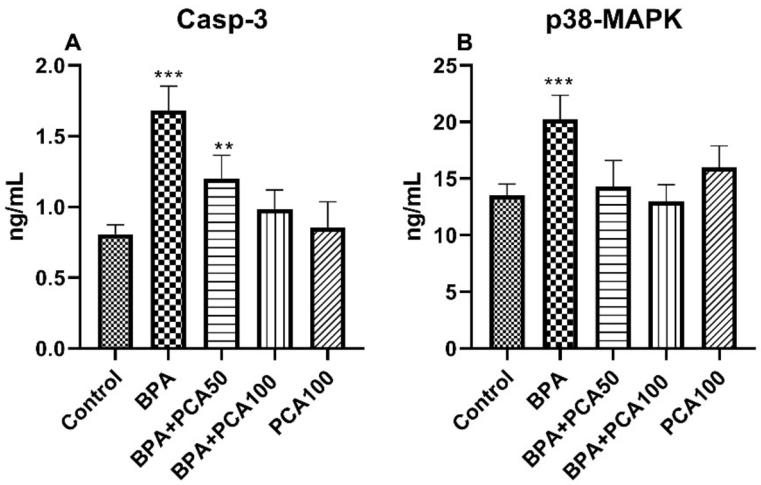

Fig. 8. Effects of BPA and PCA on Casp-3 (**A**) and p38-MAPK (**B**) levels in the experimental groups (significant differences between the control group and the other groups are shown with symbols). ***, $^{**}p < 0.01$, $^{*}p < 0.05$, $n = 10$.

is specified as 2.381 angstroms within the active site of COX-1. This information suggested a specific binding interaction between BPA and COX-1 at this site of the enzyme's active site (Fig. 10). Our analyses revealed a root mean square deviation (RMSD) of 3.157, accompanied by the formation of five hydrogen bonds. This interaction involves two ligand atoms and two receptor atoms. Importantly, our findings indicate a dock score of −6.2 kcal/mol.

Interaction analysis of the BPA-COX-1 complex

According to the information presented in Table 2; Fig. 11, which illustrates the hydrogen interactions within the BPA-COX-1 active site complex, multiple residues (ARG 49 A, ALA 133 A, and THR 322B) actively participate in the formation of hydrogen bonds with BPA. The measured distances between hydrogen and acceptor atoms (H-A and D-A) fall within the conventional range for hydrogen bonding, indicating robust and stable interactions. Furthermore, the angles formed by the donor atoms exhibit a configuration conducive to favorable hydrogen bonding geometry, reinforcing the robust nature of these interactions. Notably, ASP 135 A and TYR 136 A engage in hydrophobic interactions within the BPA-COX-1 complex (Table 3). The proximity between the ligand atom and the protein atom conforms to the typical range for hydrophobic interactions, suggesting a durable association. Given their propensity to increase the stability of protein–ligand complexes, hydrophobic interactions play a pivotal role in determining the overall binding affinity. These findings offer valuable insights into the molecular interactions and potential inhibitory effects of BPA on the activity of COX-1.

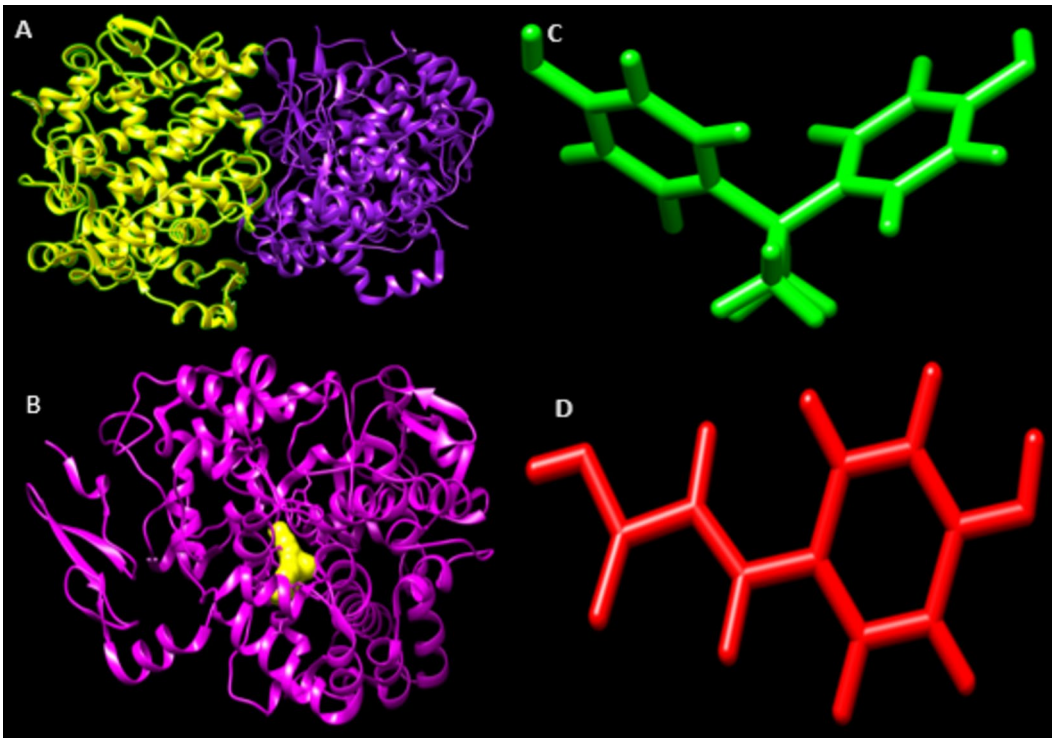

Fig. 9. X-ray crystal coordinates of COX-1 (PDB: 3N8Z) (**A**); 3D structure of BPA (**B**) Docking complex BPA-COX-1; 3D image taken by PyMOL software (**C**); 3D structure of PCA (**D**).

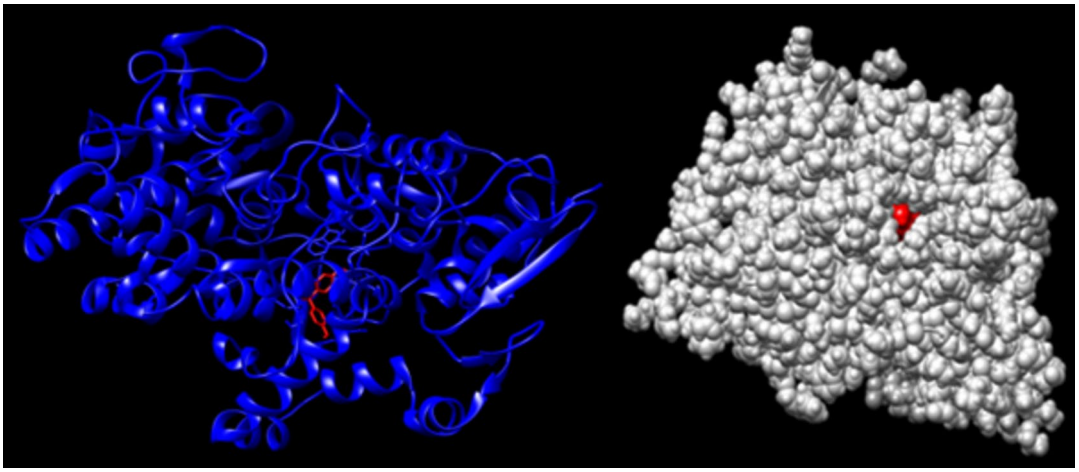

Fig. 10. BPA-COX-1 complex docking (hydrogen bond with THR 322. B, pos 8, 2.381 Å within the COX-1 active site), 3D images were taken with UCSF Chimera software.

Index	Residue	AA	Distance H-A	Distance D-A	Donor angle	Protein donor	Side chain
1	49 A	ARG	2.50	3.29	136.77	V	V
2	133 A	ALA	2.30	3.16	152.04	X	X
3	322B	THR	2.67	3.01	101.36	V	V
4	322B	THR	2.29	3.21	168.82	X	X

Table 2. Hydrogen interactions between BPA and the COX1 complex.

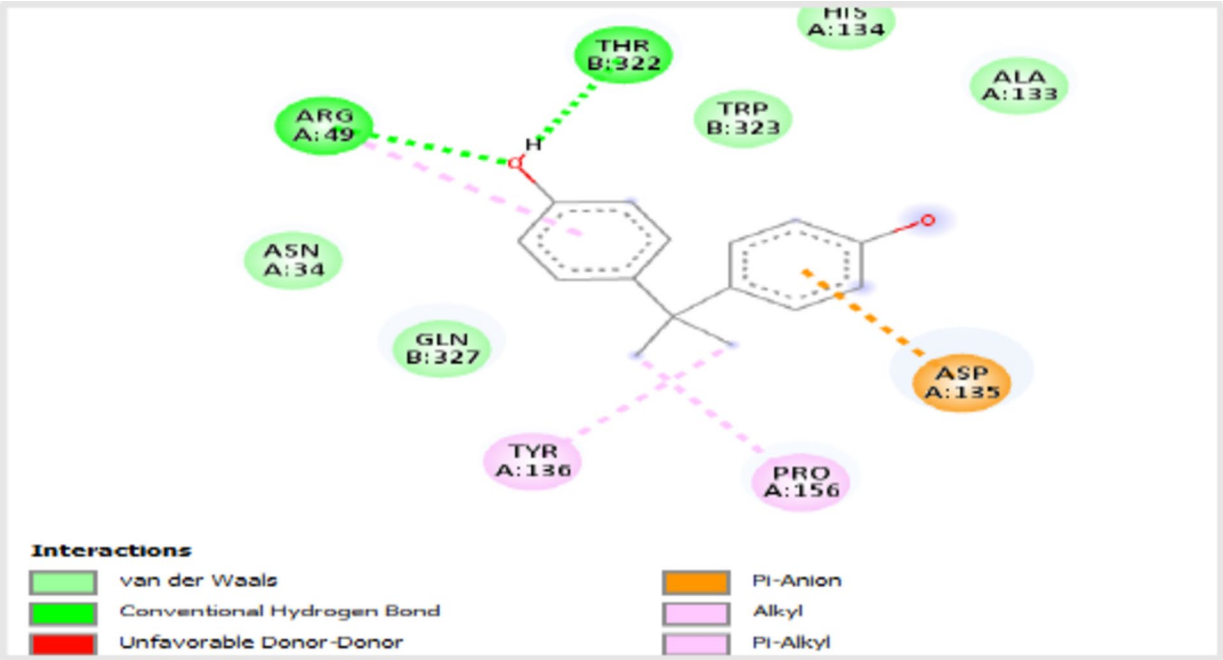

Fig. 11. Interaction analysis of the BPA-COX-1 complex (2D).

Index	Residue	AA	Distance H-A	Ligand atom	Protein atom
1	135 A	ASP	3.60	8993	851
2	136 A	TYR	3.60	8993	862
3	136 A	TYR	3.70	8994	864

Table 3. Hydrophobic interactions between BPA and the COX1 complex.

Molecular decoding perspective of BPA and PCA interactions

The results of the computational analysis revealed an unprecedented chemical interaction between BPA and PCA, featuring two hydrogen bonds with a confirmed short distance indicative of a stable ligand-ligand interaction (Fig. 12). This in silico revelation offers a unique perspective on the potential chemical contributions of similar interactions to the overarching protective mechanism, providing insights into analogous protective actions for the ultimate outcome.

Molecular docking of PCA/KEAP1 and the PCA/TNF trimer

The interaction of PCA with KEAP1 was determined by the docking score (−4.98722) and glide energy (−26.1918). Higher negative values indicate that the ligand binds more robustly to the receptor and forms a stable complex. The interaction of PCA with the TNF trimer was determined by the docking score (−6.92274) and glide energy (−29.6087). Similarly, more negative scores indicate intact ligand binding with the TNF trimer. The high negative docking scores for PCA with both KEAP1 and TNF trimers imply robust interactions between this ligand and these proteins, suggesting potential therapeutic applications. Subsequent experimental analyses, as depicted in Fig. 13; Table 4, validated our computational findings.

Several notable molecular interactions were identified via PCA and KEAP1 molecular docking analysis. A hydrogen bond was established between ARG 415 and H:2916-O:4418, with a distance of 1.83 Å. Another hydrogen bond was observed between ARG 415 and H:2920-O:4418, with a distance of 1.90 Å. A pure bridge interaction with ARG 415 was identified between N712-O:4418, spanning a distance of 2.75 Å. In addition to hydrogen bonds, aromatic hydrogen bonds were recognized with ILE 416 and VAL 463 at distances of 2.53 Å and 2.74 Å between O:716-H:4429 and O:1082-H:4429, respectively. Furthermore, a hydrogen bond was detected between ARG 512 and H:3639-O:4417 at a distance of 2.79 Å. Aromatic hydrogen bonds with LEU 557 were established between O:1822-H:4432 and O:1822-H:4430 at distances of 2.68 Å and 2.77 Å, respectively (Fig. 13 (A2) and Table 5).

These findings demonstrate the formation of multiple hydrogen bonds and aromatic interactions between PCA and KEAP1. Notably, the stable binding of PCA with KEAP1 is highlighted by hydrogen bonds with ARG 415 and ARG 512 (Fig. 13 (A2) and Table 5).

During the molecular docking analysis of PCA with the TNF trimer, an aromatic hydrogen bond with LEU 120 was identified at a distance of 2.67 Å between O:790-H:6541. Additionally, an aromatic hydrogen

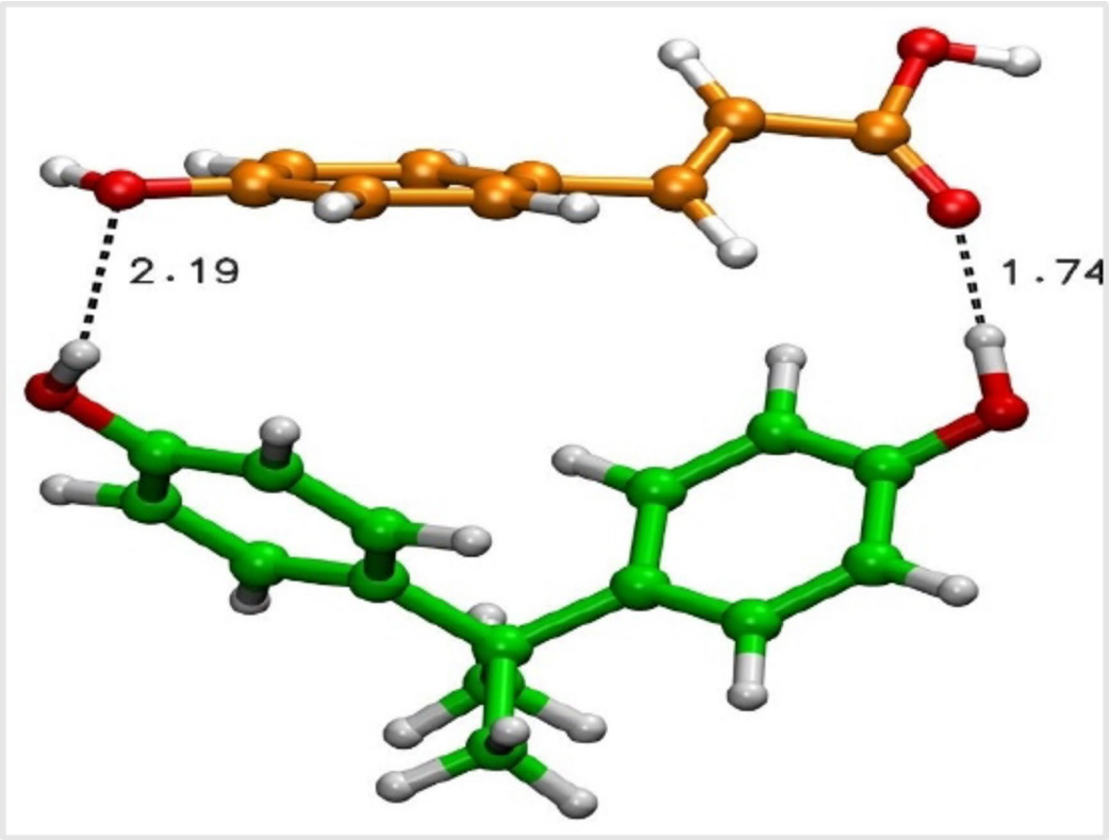

Fig. 12. Close-up snapshots of the interaction sites of the optimized structure of BPA-PCA. Color code; BPA: green, PCA: orange.

bond with TRY 119 occurred between H:6035-H:6529 at a distance of 2.65 Å. Hydrogen bonds with TRY 151 were established between H:6267-O:6528 and O:1039-H:6545, manifesting at distances of 1.95 Å and 1.97 Å, respectively (Fig. 13 (B2) and Table 5). These outcomes substantiated the formation of hydrogen bonds, particularly aromatic hydrogen bonds, between PCA and the TNF trimer. These interactions suggest potential therapeutic implications by providing a robust ligand binding mechanism (Fig. 13 (B2) and Table 5).

MM-GBSA analyses

PCA/KEAP1 MM-GBSA analysis

r_psp_MMGBSA_dG_Bind: This value is a measure of the binding free energy, and its relatively large negative value (−63.78) indicates a favorable binding interaction between the molecules. **r_psp_MMGBSA_dG_Bind_Coulomb**: A negative value (−37.74) indicates a significant contribution from Coulomb interactions and emphasizes the role of electrostatic forces in binding. **r_psp_MMGBSA_dG_Bind_Covalent**: With a large positive value (1340.55), this component indicates a significant covalent contribution to the binding free energy. **r_psp_MMGBSA_dG_Bind_Hbond**: A negative value (−29,90) indicates a positive contribution from hydrogen bonding interactions in the binding process. **r_psp_MMGBSA_dG_Bind_Lipo**: This term, with a large negative value (−12,365.56), implies a significantly positive contribution from lipophilic (hydrophobic) interactions in binding. **r_psp_MMGBSA_dG_Bind_Packing**: A negative value (−10,046.64) indicates that packing interactions play a crucial role in the stabilization of the binding complex. A negative value of **r_psp_MMGBSA_dG_Bind_SelfCont** (−818.87) indicates that the binding process is relatively self-sufficient and does not require any significant external influence. **r_psp_MMGBSA_dG_Bind_Solv_GB**: A negative value (−35,36) indicates that electrostatic interactions of the solvent positively contribute to the binding free energy. **r_psp_MMGBSA_dG_Bind_Solv_SA**: This term (−31,33) represents the contribution from the solvent accessible surface area and indicates its relevance in the binding process. **r_psp_MMGBSA_dG_Bind_vdW**: A negative value (−1195,47) indicates a significantly positive contribution from van der Waals interactions in binding.

PCA/TNF trimer MM-GBSA analysis

r_psp_MMGBSA_dG_Bind: −23.37—This value represents the binding energy, and a negative value indicates a positive binding interaction between the molecules. **r_psp_MMGBSA_dG_Bind_Coulomb**: −19.44—This value represents the contribution of Coulomb interactions to the binding energy, and a negative value indicates that electrostatic interactions have a significant positive effect on binding. **r_psp_MMGBSA_dG_Bind_Covalent**: −14.66—This value represents the contribution of covalent interactions to the binding energy. A negative value

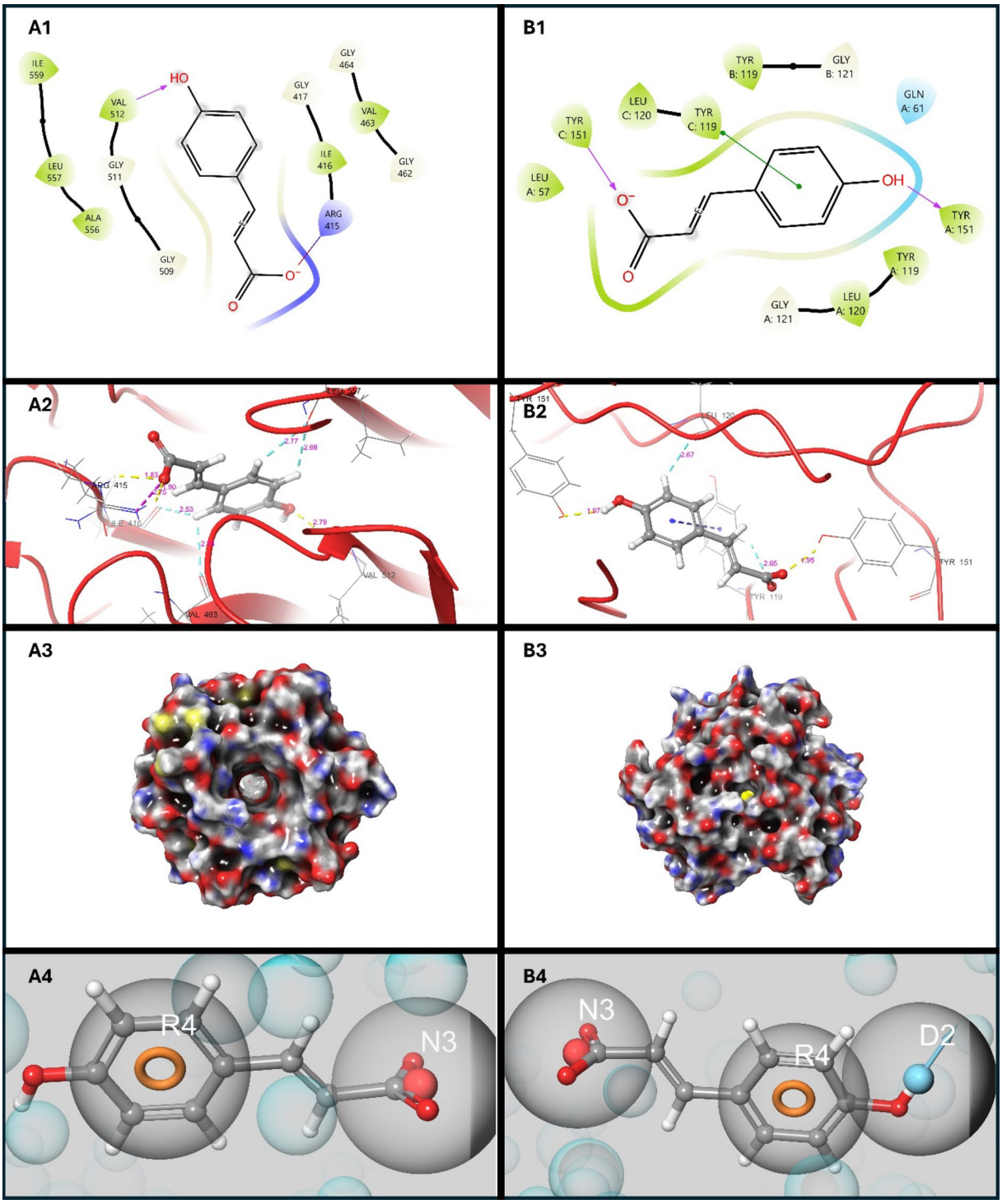

Fig. 13. (**A1**) P-Coumaric Acid/KEAP1 Molecular Docking 2D Image, (**A2**) P-Coumaric Acid/KEAP1 Molecular Docking 3D Image, (**A3**) P-Coumaric Acid/KEAP1 Molecular Docking Surface Image, (**A4**) P-Coumaric Acid/KEAP1 Pharmacophore Mapping 3D Image, (**B1**) P-Coumaric Acid/TNF Trimer Molecular Docking 2D Image, (**B2**) P-Coumaric Acid/TNF Trimer Molecular Docking 3D Image, (**B3**) P-Coumaric Acid/TNF Trimer Molecular Docking Surface Image, (**B4**) P-Coumaric Acid/TNF Trimer Pharmacophore Mapping 3D Image.

indicates that covalent interactions stabilize binding. **r_psp_MMGBSA_dG_Bind_Hbond**: −1.37—This value represents the positive influence of hydrogen bonds on the binding process. **r_psp_MMGBSA_dG_Bind_Lipo**: −13.11—This value indicates the significant contribution of lipophilic (hydrophobic) interactions to the binding energy. **r_psp_MMGBSA_dG_Bind_Packing**: 0.20—The contribution of packing interactions to the binding

Docking scores	PCA/KEAP1	PCA/TNF trimer
r_i_docking_score	−4.98722	−6.92274
r_i_glide_energy	−26.1918	−29.6087

Table 4. Molecular docking scores of PCA/KEAP1 and the PCA/TNF trimer.

Docking complex	Bond + amino acid	Atom1 (Receptor)	Atom2 (Ligand)	Distance (Angstrom= Å)
PCA/KEAP1	Hydrogen bond with ARG 415	H:2916	O:4418	1.83 Å
	Hydrogen bond with ARG 415	H:2920	O:4418	1.90 Å
	Salt bridge with ARG 415	N712	O:4418	2.75 Å
	Aromatic H bond with ILE 416	O:716	H:4429	2.53 Å
	Aromatic H bond with VAL 463	O:1082	H:4429	2.74 Å
	Hydrogen bond with ARG 512	H:3639	O:4417	2.79 Å
	Aromatic H bond with LEU 557	O:1822	H:4432	2.68 Å
	Aromatic H bond with LEU 557	O:1822	H:4430	2.77 Å
PCA/TNF trimer	Aromatic H bond with LEU 120	O:790	H:6541	2.67 Å
	Aromatic H bond with TRY 119	H:6035	H:6529	2.65 Å
	Hydrogen bond with TRY 151	H:6267	O:6528	1.95 Å
	Hydrogen bond with TRY 151	O:1039	H:6545	1.97 Å

Table 5. Molecular docking analysis: distances between ligand-binding amino acids and atoms.

Features	PCA/KEAP1		PCA/TNF trimer		
Rank	1	2	1	2	3
Feature_label	N3	R4	R4	D2	N3
Score	−1.31	−0.60	−1.34	−0.66	−0.32
X	−90.9677	−91.329	−7.6272	−5.2617	−11.3591
Y	107.3013	102.4028	3.8024	6.0073	−0.6656
Z	−9.0726	−5.8461	−15.1842	−15.9108	−15.9599
Type	N	R	R	D	N
Num	2	3	3	1	2
From_chemscore	0	0	0	0	0
Source	HBond	RingChemscoreHphobe	RingChemscoreHphobe	HBond	HBond

Table 6. Pharmacophore mapping analysis results (A = acceptor, D = donor, H = hydrophobic, N = negative ionic, P = positive ionic, R = aromatic ring).

energy is positive but relatively low. **r_psp_MMGBSA_dG_Bind_SelfCont**: 4.24—Indicates that the binding process is self-sufficient and does not require external interactions. **r_psp_MMGBSA_dG_Bind_Solv_GB**: 27.42—Indicates the positive contribution of electrostatic interactions of the solvent to the binding energy. **r_psp_MMGBSA_dG_Bind_Solv_SA**: −6.65—The contribution of the solvent surface area to the binding energy is negative, indicating that solvent interactions stabilize binding. **r_psp_MMGBSA_dG_Bind_vdW**: 0.06—The contribution of van der Waals interactions to the binding energy is positive but relatively low.

These values evaluate in detail the contributions of molecular interactions to the binding energy and provide information about the thermodynamic properties of this molecular system. Negative values generally represent interactions that stabilize binding, whereas positive values represent interactions that make binding difficult.

Pharmacophore mapping

This dataset encompasses the outcomes of a comprehensive pharmacophore mapping analysis, providing insights into the intricate interactions between the PCA molecule and the KEAP1 and TNF trimer receptors. The results serve as a condensed representation of the findings derived from the pharmacophore mapping analysis, shedding light on the nuanced interactions of PCA with the specified receptors (Fig. 13 (A4–B4) and Table 6).

Molecular dynamics

Molecular dynamics analysis

Ligand–protein interaction dynamics

The root mean square deviation (RMSD) graph at 100 ns (Fig. 14 (C1) and (D1)) illustrates variations in ligand–protein interactions with respect to the protein backbone. This finding suggested a potential impact of PCA on the dynamics of both KEAP1 and the TNF trimer.

Complex protein–ligand interactions

An intricate network of interactions, including Hydrogen Bonds, Hydrophobic, Ionic, and Water Bridges, unfolds between PCA and KEAP1 and TNF Trimer (Fig. 14 (C2) and 10 (D2)). This detailed examination identifies specific atoms involved in these binding modes, revealing molecular recognition processes.

Ligand–protein dynamic fluctuation (RMSF) graphs

Figure 14 (C3) and 10 (D3) show the dynamic interactions of PCA with KEAP1 and the TNF trimer throughout the simulation. The fluctuations in the protein backbone underscore the adaptability of the PCA binding site to both KEAP1 and the TNF trimer.

Schematic representation of ligand–atom interactions

Visualizing the detailed interactions between ligand atoms and specific protein residues (Fig. 14 (C4) and 10 (D4)) enhances the understanding of the molecular binding mechanism. This schematic elucidates fundamental interactions influencing the stability of the KEAP1 complex with PCA. Therefore, our in-depth molecular dynamics analysis provides insights into the dynamic nature of PCA binding to KEAP1 and the TNF trimer. These interactions, as revealed through RMSD, protein–ligand communications, RMSF, and detailed schematics, contribute to understanding the regulatory mechanisms and therapeutic potential of PCA in modulating KEAP1/NRF2/ARE pathway activation and TNFα inhibition (Fig. 14).

Histopathological findings

Upon histopathological examination of liver tissues, normal histological appearances were noted in the control and PCA100 groups. Conversely, the BPA group exhibited severe degeneration and necrosis of hepatocytes, along with sinusoidal dilatation and vascular hyperemia. The BPA + PCA50 group displayed moderate hepatocellular degeneration, mild necrosis, sinusoidal dilatation, and severe vascular hyperemia. Mild hepatocellular degeneration and hyperemia in vessels were observed in the BPA + PCA100 group (Fig. 15). The histopathological findings, along with the corresponding scores and statistical analyses, are detailed in Fig. 16.

Immunohistochemical findings

During immunohistochemical examination of liver tissues, pro-apoptotic Bax expression was assessed as negative in the control and PCA groups. Conversely, the BPA group presented intense intracytoplasmic Bax expression in hepatocytes. The BPA + PCA50 group presented moderate levels of Bax expression, whereas the BPA + PCA100 group presented mild Bax expression in hepatocytes (Fig. 17). A statistically significant difference ($p < 0.05$) was observed compared with that in the BPA group. The detailed immunohistochemical staining data and statistical analysis findings are presented in Fig. 18.

Immunofluorescence staining

Further immunofluorescence staining of hepatic tissues was performed to evaluate the extent of the hepatocellular insult induced by BPA administration. The expression levels of the cellular stress mediators JNK and PERK were evaluated as negative in the control and PCA groups. In the BPA group, marked intracytoplasmic JNK and PERK expression was observed in hepatocytes. Moderate levels of JNK and PERK expression were detected in hepatocytes in the BPA + PCA50 group. In the BPA + PCA100 group, low JNK and PERK expression was detected in hepatocytes (Fig. 19). The immunofluorescence staining data and statistical analysis results are presented in Fig. 18.

Discussion

BPA, a widely employed endocrine-disrupting agent found in industrial polycarbonate plastics, elicits receptor-like responses, thereby perturbing hormone levels and metabolic pathways across diverse cell populations[49,50]. Notably, the liver manifests heightened sensitivity to even minimal BPA exposure relative to other organs, necessitating focused investigations into its hepatic ramifications[51]. This study investigated the effects of BPA-induced precipitation of hepatocellular insult in a rat model by assessing the potential mitigatory effects of PCA. By revealing the molecular mechanism underlying the substantial disruptions in hepatocellular redox equilibrium, coupled with the increased expression of proinflammatory mediators and increased apoptotic indices, our findings underscore the notable biochemical protective effects of PCA against BPA-induced hepatic insult.

Consistent body weights across the experimental groups during the acute duration of the experiment suggested that BPA and PCA had minimal impacts on animal health or growth during the acute duration of the experiment. Likewise, stable liver weights indicate that the treatments did not induce noticeable changes in organ size.

Moreover, BPA, along with its glucuronide conjugate, has been implicated in increasing liver ROS levels, thereby stimulating oxidative stress that disrupts fundamental cellular processes, notably lipid cell membrane peroxidation. This phenomenon leads to the release of MDA, an indirect indicator of cellular damage and

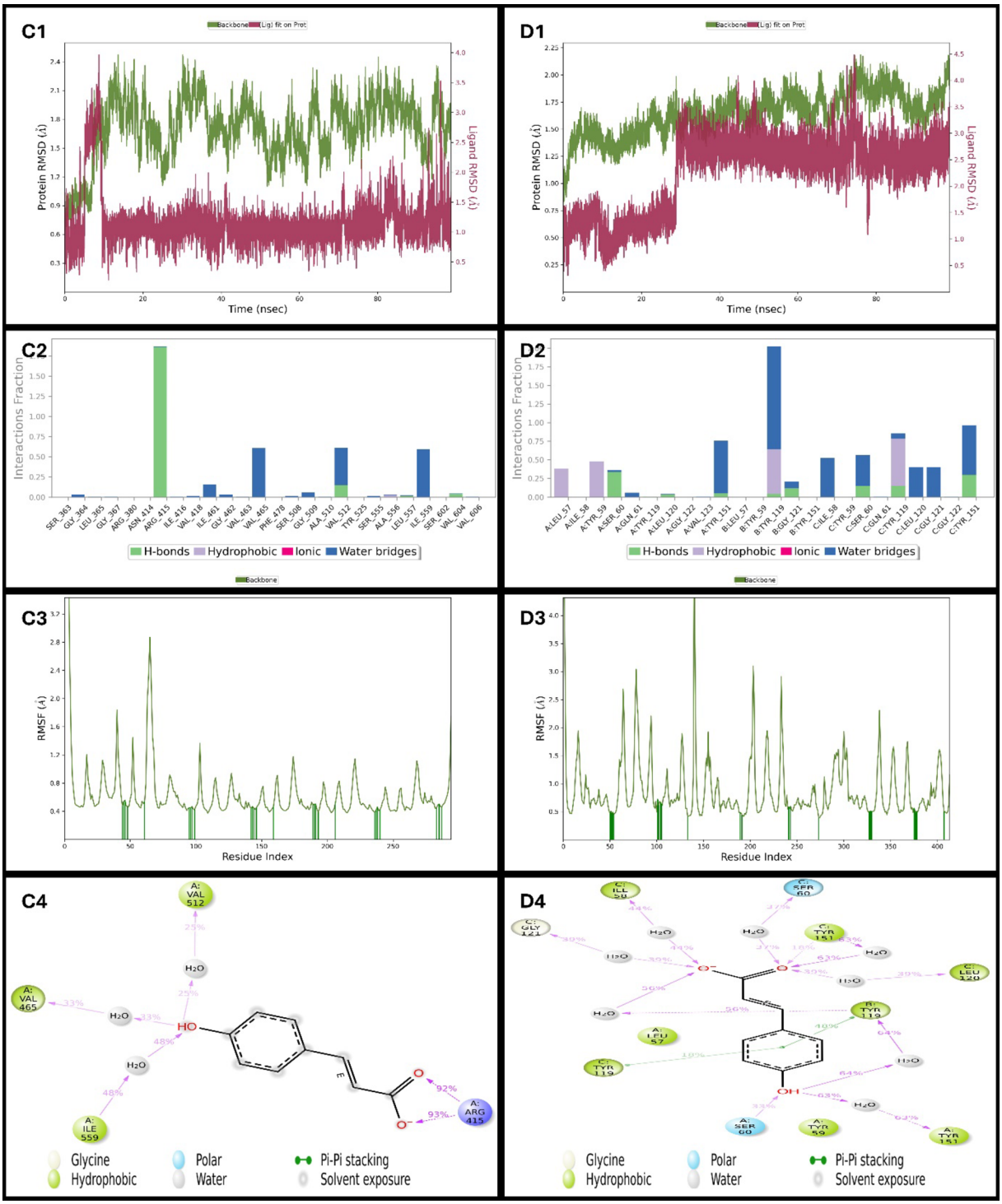

Fig. 14. (**C1**) P-coumaric acid/NRF2, root mean square deviation (RMSD); (**C2**) P-coumaric acid/NRF2, protein–ligand interactions (hydrogen bonds, hydrophobic, ionic and water bridges); (**C3**) P-coumaric acid/NRF2, root mean square fluctuation (RMSF); (**C4**) P-coumaric acid/NRF2, schematic of detailed ligand-atom interactions with protein residues; (**D1**) P-coumaric acid/TNF trimer, root mean square deviation (RMSD); (**D2**) P-coumaric acid/TNF trimer protein–ligand contacts (hydrogen bonds, hydrophobic, ionic and water bridges); (**D3**) P-coumaric acid/TNF trimer, root mean square fluctuation (RMSF); (**D4**) P-coumaric acid/TNF trimer, A schematic of detailed ligand-atom interactions with protein residues. (Images made with Schrödinger Maestro 2023/4 licensed version).

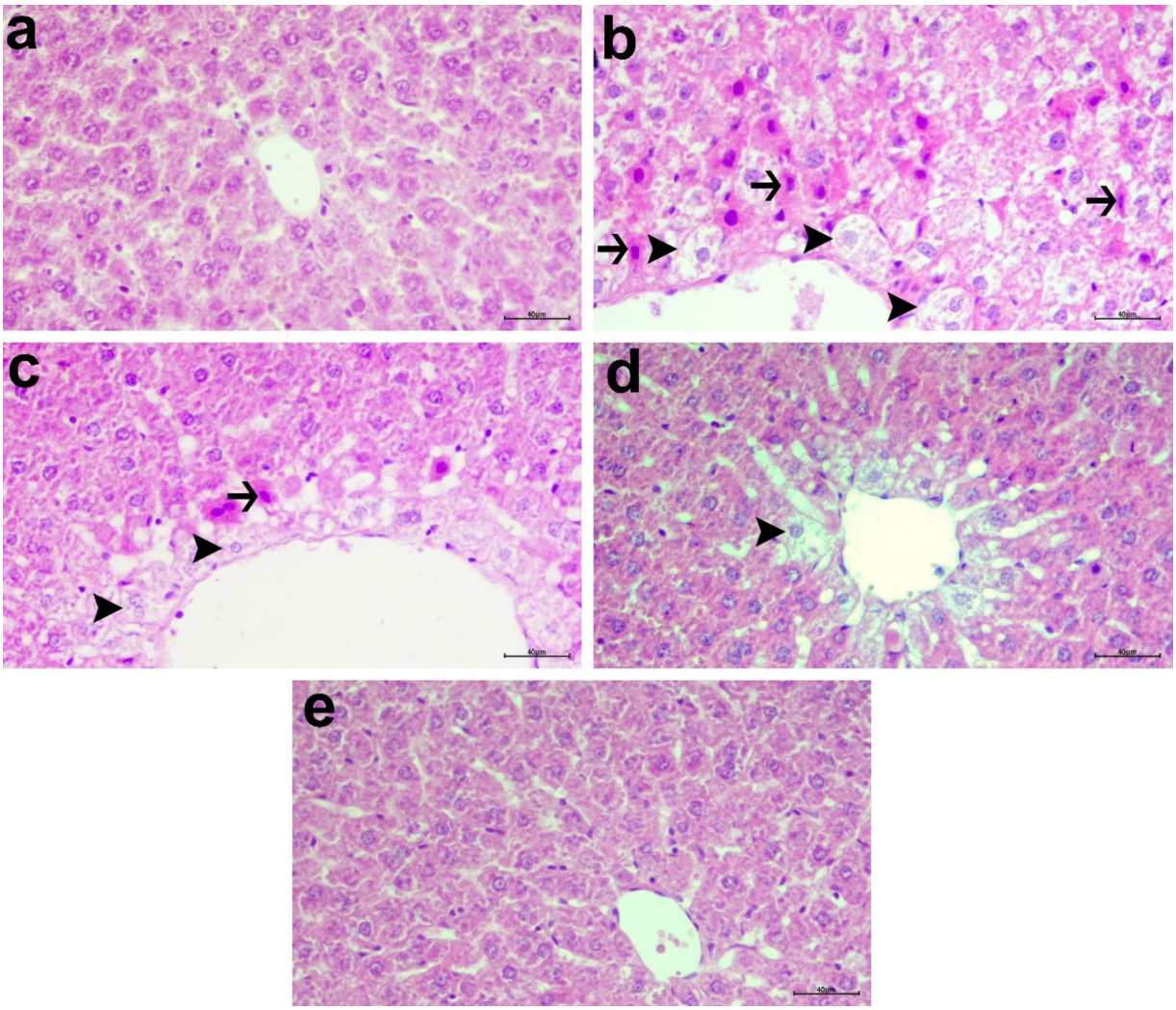

Fig. 15. Liver tissue; control (**a**), BPA (**b**), BPA + PCA50 (**c**), BPA + PCA100 (**d**) and PCA100 (**e**), degeneration (arrowheads) and necrosis (arrows) in hepatocytes, H&E, Scale bar: 40 µm.

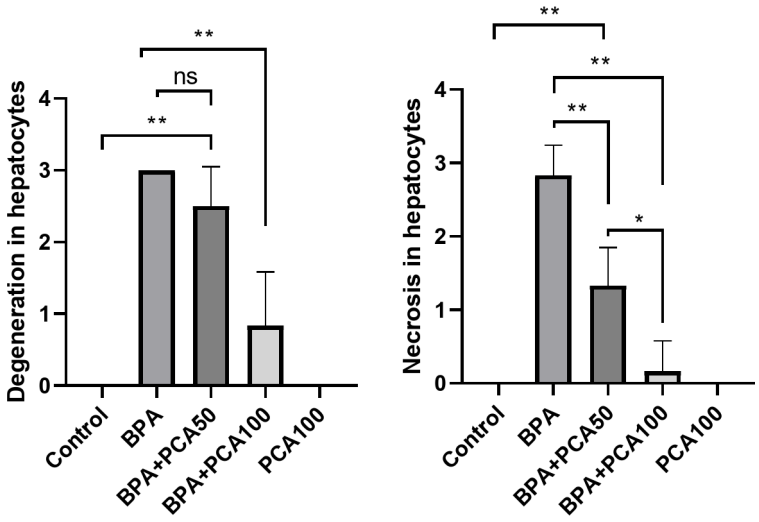

Fig. 16. Histopathological findings in liver tissue were scored, and the data were statistically analyzed. **, *: there was a significant ($p < 0.05$) difference between groups; ns: no significant difference.

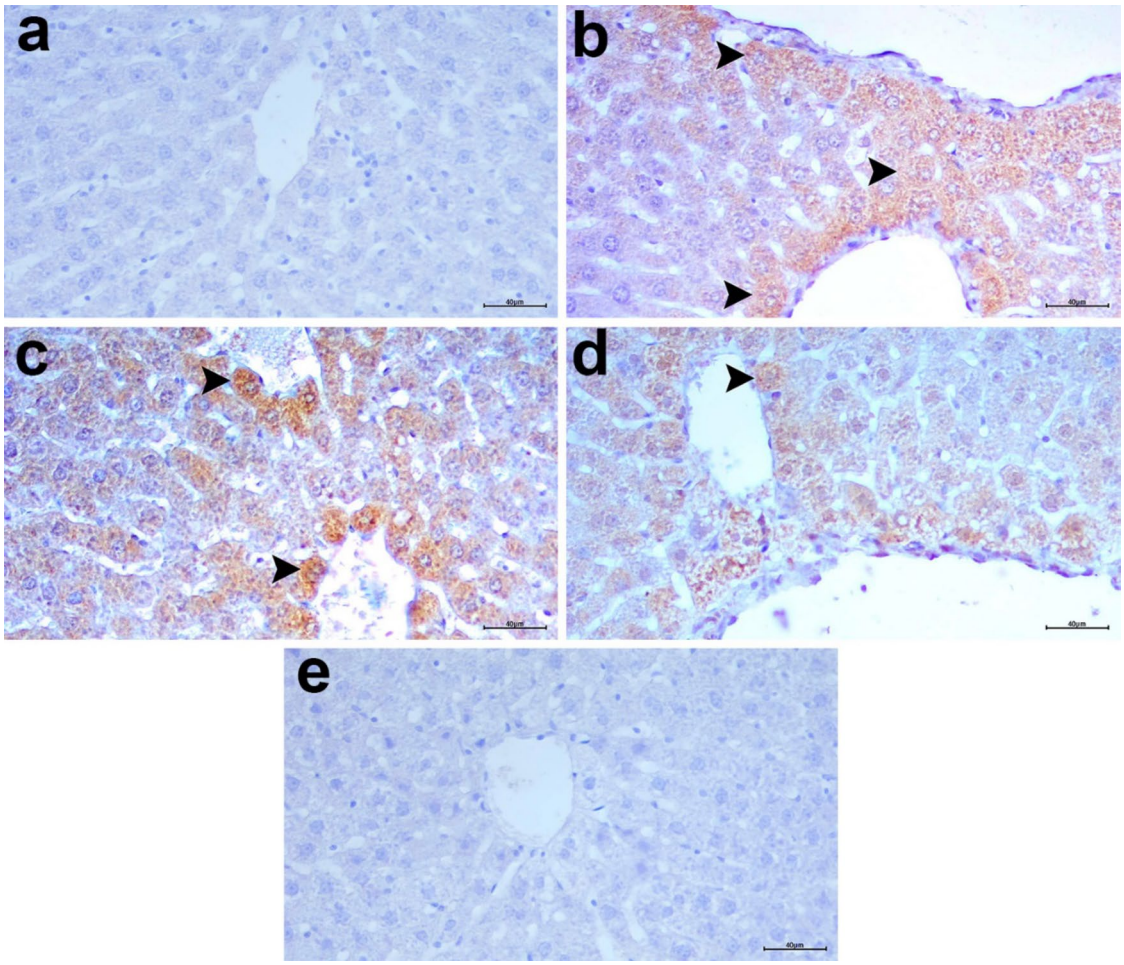

Fig. 17. Liver tissue; Control (**a**), BPA (**b**), BPA + PCA50 (**c**), BPA + PCA100 (**d**) and PCA100 (**e**), Bax expression in hepatocytes, IHC-P, scale bar: 40 µm.

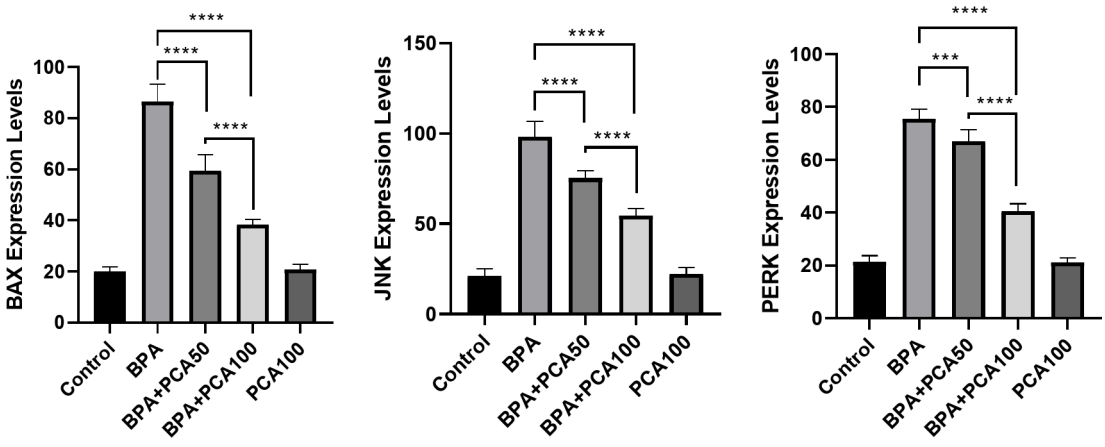

Fig. 18. Immunohistochemical and immunofluorescence staining results and statistical analysis findings in liver tissue. ****, ***There was a significant ($p < 0.0001$) difference between groups.

a principal marker of lipid peroxidation[52]. The increase in MDA levels observed in the liver tissues of BPA-treated rats signifies an increase in lipid peroxidation and oxidative stress resulting from hepatocellular insult. These findings highlight the deleterious impact of BPA on hepatic redox balance. In contrast, PCA, in a dose-dependent manner, reversed this increase in the MDA level to its control value.

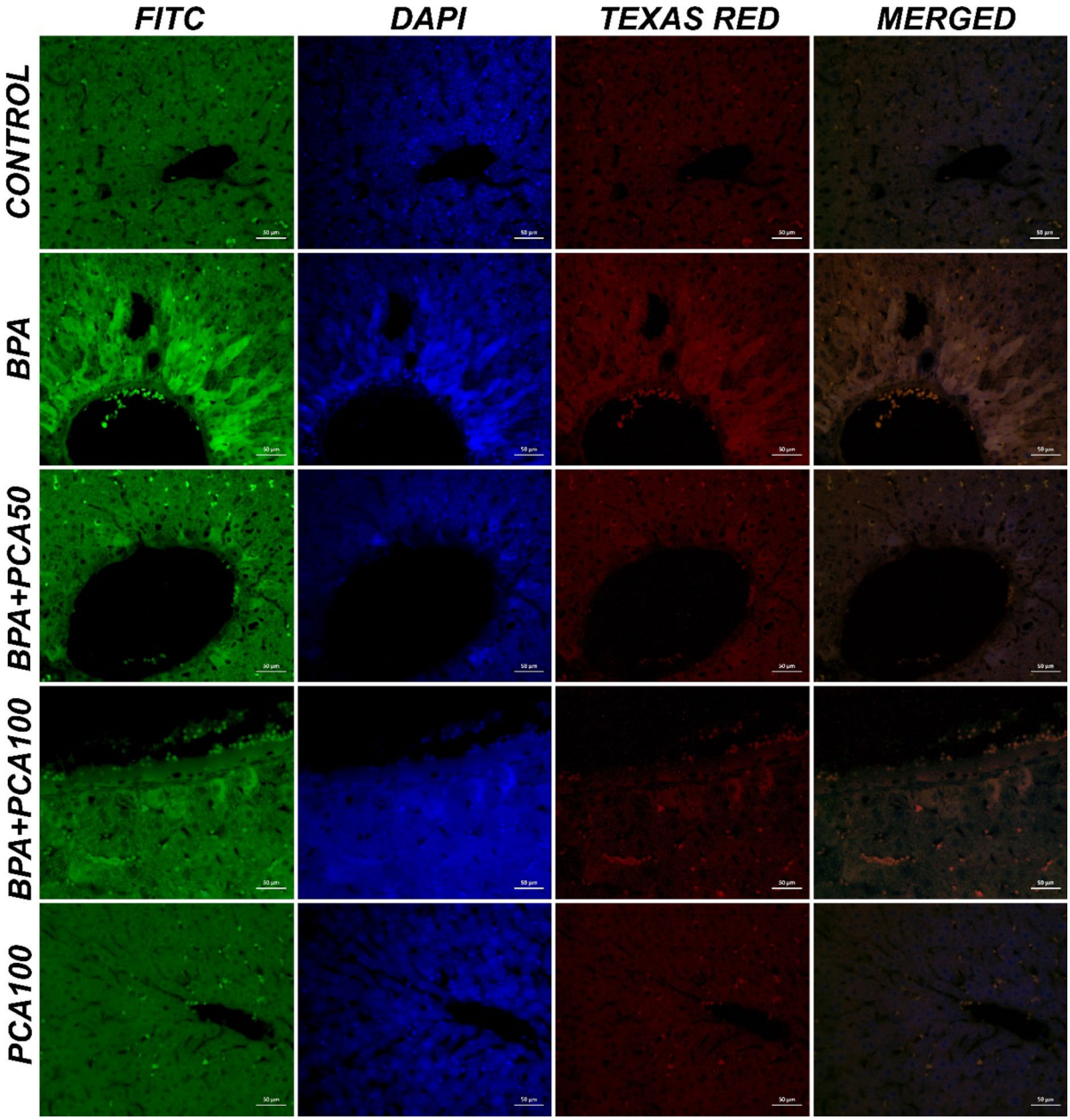

Fig. 19. Liver tissue; JNK expression (FITC) and PERK expression (TEXAS RED) in hepatocytes, IF, scale bar: 50 µm.

The levels of antioxidant markers, including SOD, GSS, GPx, and CAT, are vital intrinsic defense mechanisms against oxidative damage induced by oxygen radicals[53]. SOD primarily neutralizes superoxide radicals by converting them into less harmful hydrogen peroxide[54]. CAT, a hemoprotein, mitigates damage by converting hydrogen peroxide into water and molecular oxygen[55]. Similarly, GPx, a selenoenzyme, prevents oxidative damage by converting hydrogen peroxide to water[56]. The observed decrease in their activity levels in BPA-induced liver damage was mitigated by PCA, emphasizing its role in preserving antioxidant enzyme activities. These findings underscore the protective effects of PCA against BPA-induced oxidative stress and its potential as a nutraceutical agent with therapeutic potential for targeting hepatic injury. Consistent with our findings, a previous study revealed reduced activity of antioxidant enzymes, including CAT, SOD, GSS, and GPx, in BPA-treated rat liver tissues[57].

The involvement of nitric oxide (NO), inducible nitric oxide synthase (iNOS), and myeloperoxidase (MPO) in orchestrating oxidative stress, inflammation, and apoptosis after BPA-induced hepatic insult is crucial. NO, generated by iNOS, regulates inflammation, whereas MPO modulates iNOS activity. Studies by Mohammed et al.[18] and Lin et al.[58] revealed increased iNOS and MPO levels in BPA-treated rats and liver damage models. Our findings support these findings, indicating that PCA plays a role in moderating iNOS and MPO activity, thus mitigating inflammation.

In addition to the aforementioned redox balance parameters, the Nrf-2/HO-1 signaling pathway is a crucial indicator of intracellular oxidative damage and a key player in hepatic detoxification and defense against oxidative stress and inflammation by modulating cellular redox homeostasis. BPA exposure hampers this defense mechanism by attenuating the activity of both HO-1 and Nrf2 enzymes[59,60]. Our findings align with these observations, elucidating the suppression of the protective Nrf2/HO-1 pathway post-BPA exposure and demonstrating the dose-dependent restoration of this signaling cascade by PCA, underscoring its potential as a therapeutic intervention in mitigating BPA-induced hepatic oxidative stress.

Likewise, the dynamic interplay between oxidative stress and inflammatory mediators is integral to cellular defense mechanisms. Under physiological conditions, in addition to anti-inflammatory agents, TNF-α, IL-1β, IL-6, and NF-κB maintain the cellular balance. However, BPA exposure disrupts this balance, increasing proinflammatory marker levels and reducing anti-inflammatory cytokine levels. Notably, our study revealed that PCA administration attenuated these effects, suggesting its anti-inflammatory potential. TNF-α inhibition, facilitated by PCA, regulates inflammation by reducing TNF-α levels, thus modulating NF-κB activity and balancing cytokine levels. These results underscore the therapeutic potential of PCA for mitigating BPA-induced hepatic dysfunction[61–68].

However, while our study sheds light on the effects of BPA on proinflammatory markers and the potential for PCA-mediated modulation of inflammation, more in-depth investigation into the activation status of NF-κB would enhance our molecular understanding. Specifically, the phosphorylation of key NF-κB subunits, such as serine 536 or 276, and their regulation by upstream signaling pathways like p38 MAPK, are critical for fully unraveling the mechanisms underlying BPA-induced hepatic inflammation. These analyses are essential for advancing our understanding of the specific molecular pathways involved and warrant further exploration in future studies. Beyond these downstream effects, it is crucial to consider the upstream regulators that may contribute to the activation of inflammatory pathways in response to BPA exposure. A key factor in inflammation is the activation of pattern recognition receptors (PRRs), such as Toll-like receptors (TLRs) and NOD-like receptors (NLRs), which play pivotal roles in recognizing pathogen-associated molecular patterns and initiating immune responses. Activation of these receptors can, in turn, lead to the activation of downstream transcription factors like NF-κB, AP-1, and MAPKs as central mediators of inflammatory pathways. These pathways are often interconnected and regulate the expression of proinflammatory cytokines, such as TNF-α, IL-1β, and IL-6, which are critical for initiating and sustaining inflammation[69]. Moreover, MAPKs, including p38, JNK, and ERK, modulate the phosphorylation of key transcription factors, influencing cellular responses to stress, including those triggered by BPA. While our current study focuses primarily on the downstream effects of BPA on inflammatory markers, a deeper understanding of the upstream signaling events that activate these pathways is essential. Future research exploring the roles of PRRs and MAPKs in BPA-induced hepatic inflammation will be critical for gaining a more comprehensive understanding of the molecular mechanisms involved and could provide valuable insights into the potential modulatory effects of compounds like PCA.

In addition to the inhibition of TNF-α, the modulatory effect of PCA on the KEAP1-NRF2 system was investigated. The KEAP1-NRF2 pathway plays a crucial role in safeguarding cellular integrity by inhibiting inflammatory and apoptotic pathways that can lead to cellular damage, such as the upregulation of iNOS, COX-2, and Caspase-3[70]. KEAP1 serves as a sensor for the cellular redox state and plays a pivotal role in coordinating the cellular response to oxidative stress and exposure to toxic substances by regulating the activity of NRF2. This system contributes to maintaining cellular homeostasis and enhancing the liver's resilience against various insults.

Given the interconnected nature of oxidative stress, inflammation, and apoptosis, it is essential to explore how these pathways interact in the context of BPA-induced hepatic damage. In our study, we observed a significant increase in oxidative stress following BPA exposure, which was concomitant with heightened inflammatory responses, as evidenced by elevated levels of proinflammatory cytokines such as TNF-α, IL-1β, and IL-6. These findings are consistent with previous studies, which have highlighted the critical roles of inflammation in mediating oxidative stress-induced liver injury[71]. Furthermore, our results suggest that oxidative stress-induced inflammation may, in part, drive the apoptotic processes observed in BPA-exposed liver tissue, supporting the findings of recent literature that links oxidative stress to cellular damage and apoptosis in toxicological contexts. However, as Das et al. (2024) also noted, the exact molecular mechanisms underlying these interactions remain incompletely understood, underscoring the need for further research to clarify the direct relationships between oxidative stress, inflammation, and apoptosis in liver injury.

Consequently, further in silico detailed computational investigations were conducted to elucidate the modulatory effects of PCA on KEAP1 and the TNF trimer, aiming to identify potential therapeutic targets for mitigating hepatic injury induced by BPA. Validation through docking scores and glide energies indicated robust binding between PCA and both KEAP1 and the TNF trimer. Notably, the formation of hydrogen bonds, particularly with ARG 415 and ARG 512 in KEAP1, underscore the stability of PCA interactions. Similarly, interactions with TNF-Trimer involve hydrogen bonds, emphasizing its potential therapeutic benefits. Thermodynamic profiling via MM-GBSA highlighted favorable binding interactions, with negative values indicating stability and suggesting potential avenues for therapeutic interventions involving this nutraceutical compound. Pharmacophore mapping revealed nuanced interactions between PCA and the KEAP1/TNF trimer receptors, providing a foundation for further exploration. Molecular dynamics analysis revealed the dynamic impact of PCA on KEAP1 and the TNF trimer, shedding light on its regulatory mechanisms in inflammation and oxidative stress pathways. Overall, the combined effects of PCA on KEAP1 inhibition, NRF2 activation, and TNF alpha inhibition effectively counteract BPA-induced liver damage while preserving liver function and combating hepatotoxic stressors.

The observed increase in cellular stress and proinflammatory mediator levels triggered by BPA prompted in-depth investigations of apoptosis at the molecular level, with a focus on the upstream p38-MAPK pathway and

downstream caspase-3 signaling cascade. Consistent with previous studies examining hepatic injury[72], elevated levels of both markers were detected. Notably, PCA effectively mitigated BPA-induced apoptosis by attenuating Caspase-3 and p38-MAPK levels, highlighting its antiapoptotic effects.

Furthermore, PGs, which are synthesized by COX enzymes, are integral to inflammation and homeostasis[73]. COX-1, recognized for its hepatoprotective effects, synthesizes PGs with cytoprotective properties, whereas COX-2-derived PGs are associated with inflammation[74]. Previous studies have suggested a dichotomy in COX-1 and COX-2 functions, with debates on their inflammatory roles[73]. Interestingly, BPA has been reported to upregulate COX-1 transcription under certain conditions, potentially contributing to inflammation through its impact on constitutive COX isoforms[75].

BPA decreased COX-1 and PGE2 levels. Interestingly, concurrent administration of PCA significantly influenced COX-1 levels, suggesting a regulatory effect. This unexpected discovery diverges from the typical behavior of inflammatory mediators, indicating a unique impact of PCA on COX-1 expression. Computational modeling confirmed the competitive inhibitory effect of BPA on COX-1, with stable hydrogen and hydrophobic bonding at its active site. Our integrative computational approach highlighted the intricate molecular relationship between BPA and COX-1.

Furthermore, a thorough computational investigation of chemical ligand–ligand interactions revealed, for the first time, a potential chemical interplay between BPA and PCA, characterized by stable binding bonds. This novel insight expands the recognized hepatoprotective role of PCA by revealing its chemical interaction with BPA, thus contributing to the mitigation of BPA-induced hepatotoxic effects. Understanding such molecular interactions through computational analysis enhances our understanding of potential nutraceutical strategies for mitigating the detrimental impact of BPA on liver function. Histopathological examination confirmed severe hepatic degeneration and necrosis in BPA-treated rats, which were ameliorated by PCA. BPA induced the upregulation of Bax, which is indicative of mitochondrial-induced apoptosis, and immunohistochemical analyses confirmed increased Bax levels in liver tissue[76]. PCA has been shown to exert protective effects by downregulating Bax expression in hepatocytes[77].

Additionally, BPA exposure increased hepatic JNK activity, which is pivotal for cell stress signaling and apoptosis. Coadministration of PCA effectively attenuated these pathways, alleviating damage. These findings are consistent with those of previous studies on BPA-induced renal stress[30]. Our findings underscore the complex relationship between BPA-triggered apoptosis and cellular stress pathways in the liver, with PCA demonstrating promising mitigating effects.

Although this study focused primarily on toxicological endpoints and biomarkers associated with BPA-induced hepatic inflammation, a more detailed investigation of the specific molecular signaling pathways involved was not feasible because of resource constraints. Nonetheless, the findings from this study establish a strong foundation for future research that can delve deeper into the underlying mechanisms of BPA toxicity, providing a more comprehensive understanding of its impact on liver function.

Conclusion

Our study highlights the potential of PCA in mitigating BPA-induced hepatotoxicity through a multifaceted protective mechanism. PCA effectively preserves antioxidant markers and modulates key inflammatory and apoptotic pathways involved in BPA toxicity. Computational analyses suggest that PCA may attenuate BPA-induced inflammation by inhibiting TNF-α and modulating the KEAP1-NRF2 pathway. Notably, our findings reveal stable chemical interactions between PCA and BPA, including the inhibition of COX-1 by BPA via hydrogen bonding at its active site. These results suggest promising hepatoprotective properties of PCA, warranting further exploration as a potential therapeutic agent. However, the real-world applicability of PCA is contingent on several critical factors, including its bioavailability and pharmacokinetic profile for effective use in clinical settings. Additionally, the potential toxicity at higher doses and the long-term safety of PCA must be carefully evaluated. Therefore, these factors need thorough investigation before PCA can be considered a viable candidate for clinical use. Further preclinical and clinical studies are essential to fully assess its therapeutic potential and address the practical challenges that could impact its use in human therapies. Our study provides a valuable foundation for these future investigations and contributes to the growing body of knowledge on nutraceutical interventions for liver damage.

Data availability

The datasets used and/or analyzed during the current study are available from the corresponding author upon reasonable request.

Received: 22 October 2024; Accepted: 16 January 2025
Published online: 31 March 2025

References

1. Liao, C. & Kannan, K. A survey of bisphenol A and other bisphenol analogues in foodstuffs from nine cities in China. *Food Addit. Contam. Part A* **31**, 319–329 (2014).
2. Soares, A., Guieysse, B., Jefferson, B., Cartmell, E. & Lester, J. Nonylphenol in the environment: a critical review on occurrence, fate, toxicity and treatment in wastewaters. *Environ. Int.* **34**, 1033–1049 (2008).
3. Vandenberg, L. N., Maffini, M. V., Sonnenschein, C., Rubin, B. S. & Soto, A. M. Bisphenol-A and the great divide: a review of controversies in the field of endocrine disruption. *Endocr. Rev.* **30**, 75–95 (2009).
4. Feulner, B. & Clopath, C. Neural manifold under plasticity in a goal driven learning behaviour. *PLoS Comput. Biol.* **17**, e1008621 (2021).
5. Baladron, J., Vitay, J., Fietzek, T. & Hamker, F. H. The contribution of the basal ganglia and cerebellum to motor learning: a neuro-computational approach. *PLoS Comput. Biol.* **19**, e1011024 (2023).

6. Torbati, A. H. M. et al. Underlying interactive neural mechanism of motor learning governed by the cerebellum, the basal ganglia, and motor/sensory cortex: a review from theoretical perspective. *Neurosci. Behav. Physiol.* **54**, 347–356 (2024).
7. Tsai, W. T. Human health risk on environmental exposure to Bisphenol-A: a review. *J. Environ. Sci. Health Part C* **24**, 225–255 (2006).
8. Mikołajewska, K., Stragierowicz, J. & Gromadzińska, J. Bisphenol A—Application, sources of exposure and potential risks in infants, children and pregnant women. *Int. J. Occup. Med. Environ. Health* **28** (2015).
9. Volkel, W., Colnot, T., Csanady, G., Filser, J. & Dekant, W. Metabolism and kinetics of bisphenol A in humans at low doses following oral administration. *Chem. Res. Toxicol.* **15**, 1281–1287 (2002).
10. Richter, C. A. et al. In vivo effects of bisphenol A in laboratory rodent studies. *Reprod. Toxicol.* **24**, 199–224 (2007).
11. Wetherill, Y. B. et al. In vitro molecular mechanisms of bisphenol A action. *Reprod. Toxicol.* **24**, 178–198 (2007).
12. Maffini, M. V., Rubin, B. S., Sonnenschein, C. & Soto, A. M. Endocrine disruptors and reproductive health: the case of bisphenol-A. *Mol. Cell. Endocrinol.* **254**, 179–186 (2006).
13. Tekin, S. & Çelebi, F. Investigation of the effect of hesperidin on some reproductive parameters in testicular toxicity induced by Bisphenol A. *Andrologia* **54**, e14562 (2022).
14. Faheem, N. M., Askary, E. & Gharib, A. F. A. Lycopene attenuates bisphenol A-induced lung injury in adult albino rats: a histological and biochemical study. *Environ. Sci. Pollut Res.* **28**, 49139–49152 (2021).
15. Jiang, W., Zhao, H., Zhang, L., Wu, B. & Zha, Z. Maintenance of mitochondrial function by astaxanthin protects against bisphenol A-induced kidney toxicity in rats. *Biomed. Pharmacother.* **121**, 109629 (2020).
16. Kazemi, S. et al. Low dose administration of Bisphenol A induces liver toxicity in adult rats. *Biochem. Biophys. Res. Commun.* **494**, 107–112 (2017).
17. Hassani, F. V., Mehri, S., Abnous, K., Birner-Gruenberger, R. & Hosseinzadeh, H. Protective effect of crocin on BPA-induced liver toxicity in rats through inhibition of oxidative stress and downregulation of MAPK and MAPKAP signaling pathway and miRNA-122 expression. *Food Chem. Toxicol.* **107**, 395–405 (2017).
18. Mohammed, E. T. et al. Ginger extract ameliorates bisphenol A (BPA)-induced disruption in thyroid hormones synthesis and metabolism: involvement of Nrf-2/HO-1 pathway. *Sci. Total Environ.* **703**, 134664 (2020).
19. Peerapanyasut, W., Kobroob, A., Palee, S., Chattipakorn, N. & Wongmekiat, O. Activation of sirtuin 3 and maintenance of mitochondrial integrity by N-acetylcysteine protects against bisphenol A-induced kidney and liver toxicity in rats. *Int. J. Mol. Sci.* **20**, 267 (2019).
20. Oluranti, O. I., Alabi, B. A., Michael, O. S., Ojo, A. O. & Fatokun, B. P. Rutin prevents cardiac oxidative stress and inflammation induced by bisphenol A and dibutyl phthalate exposure via NRF-2/NF-κB pathway. *Life Sci.* **284**, 119878 (2021).
21. Wang, K., Zhao, Z. & Ji, W. Bisphenol A induces apoptosis, oxidative stress and inflammatory response in colon and liver of mice in a mitochondria-dependent manner. *Biomed. Pharmacother.* **117**, 109182 (2019).
22. Elswefy, S. E. S., Abdallah, F. R., Atteia, H. H., Wahba, A. S. & Hasan, R. A. Inflammation, oxidative stress and apoptosis cascade implications in bisphenol A-induced liver fibrosis in male rats. *Int. J. Exp. Pathol.* **97**, 369–379 (2016).
23. Jiang, K., Li, L., Long, L. & Ding, S. Comparison of alkali treatments for efficient release of p-coumaric acid and enzymatic saccharification of sorghum pith. *Bioresour. Technol.* **207**, 1–10 (2016).
24. Pragasam, S. J., Murunikkara, V., Sabina, E. P. & Rasool, M. Ameliorative effect of p-coumaric acid, a common dietary phenol, on adjuvant-induced arthritis in rats. *Rheumatol. Int.* **33**, 325–334 (2013).
25. Pei, K., Ou, J., Huang, J. & Ou, S. p-Coumaric acid and its conjugates: dietary sources, pharmacokinetic properties and biological activities. *J. Sci. Food Agric.* **96**, 2952–2962 (2016).
26. Tekin, S., Dag, Y., Bolat, M. & Sengul, E. Ratlarda Bisphenol a ile İndüklenen nefrotoksisitede kidney injury Molecule-1 Üzerine p-Kumarik Asitin Etkileri. *Laboratuvar Hayvanları Bilimi Ve Uygulamaları Dergisi* **1**, 1–7 (2021).
27. Behmanesh, M. A., Najafzadehvarzi, H. & Poormoosavi, S. M. J. C. J. Protective effect of aloe vera extract against bisphenol A induced testicular toxicity in Wistar rats. *Cell. J.* **20**, 278 (2018).
28. Güleş, Ö. et al. Protective effect of coenzyme Q10 against bisphenol-A-induced toxicity in the rat testes. *Toxicol. Ind. Health.* **35**, 466–481 (2019).
29. Oyeleye, S. I., Adefegha, S. A., Dada, F. A., Okeke, B. M. & Oboh, G. Effect of p-coumaric acid on the erectogenic enzyme activities and non-protein thiol level in the penile tissue of normal and doxorubicin-induced oxidative stress male rat. *Andrologia* **51**, e13281 (2019).
30. Tekin, S. et al. Molecular insights into the antioxidative and anti-inflammatory effects of P-coumaric acid against bisphenol A-induced testicular injury: in vivo and in silico studies. *Reprod. Toxicol.* **125**, 108579 (2024).
31. Kim, S. et al. PubChem 2023 update. *Nucleic Acids Res.* **51**, D1373–D1380 (2023).
32. PerkinElmer *ChemBioDraw Ultra 12*. https://chemistrydocs.com/chemdraw-ultra-12-0/ (2023).
33. Bank, P. D. *PDB ID: 3K9V*. https://www.rcsb.org/ (2023).
34. Pettersen, E. F. et al. UCSF Chimera—a visualization system for exploratory research and analysis. *J. Comput. Chem.* **25**, 1605–1612 (2004).
35. Shapovalov, M. V. & Dunbrack, R. L. J. S. A smoothed backbone-dependent rotamer library for proteins derived from adaptive kernel density estimates and regressions. *Structure* **19**, 844–858 (2011).
36. Tian, W., Chen, C., Lei, X., Zhao, J. & Liang, J. J. CASTp 3.0: computed atlas of surface topography of proteins. *Nucleic Acids Res.* **46**, W363–W367 (2018).
37. Trott, O. & Olson, A. J. AutoDock Vina: improving the speed and accuracy of docking with a new scoring function, efficient optimization, and multithreading. *J. Comput. Chem.* **31**, 455–461 (2010).
38. Schrodinger, L. (2023).
39. Adasme, M. F. et al. PLIP: Expanding the scope of the protein–ligand interaction profiler to DNA and RNA. *Nucleic Acids Res.* **49**, W530–W534 (2021).
40. BIOVIA, D. S. J. C. Discovery Studio Visualizer; v21. 1.0. 20298 Dassault Systèmes (2021).
41. Kim, S. et al. PubChem in 2021: new data content and improved web interfaces. *Nucleic Acids Res.* **49**, D1388–D1395 (2021).
42. Zhao, Y. & Truhlar, D. G. The M06 suite of density functionals for main group thermochemistry, thermochemical kinetics, noncovalent interactions, excited states, and transition elements: two new functionals and systematic testing of four M06-class functionals and 12 other functionals. *Theor. Chem. Acc.* **120**, 215–241 (2008).
43. Frisch, A. J. W. Gaussian 09 W Reference. 470 (2009).
44. Hasanat, A. et al. Antinociceptive activity of Macaranga denticulata Muell. Arg. (family: Euphorbiaceae): in vivo and in silico studies. *Medicines* **4**, 88 (2017).
45. Chaudhari, P. & Bari, S. J. M. D. In silico exploration of c-KIT inhibitors by pharmaco-informatics methodology: pharmacophore modeling, 3D QSAR, docking studies, and virtual screening. *Mol. Divers.* **20**, 41–53 (2016).
46. Fatima, A. et al. Exploring quantum computational, molecular docking, and molecular dynamics simulation with MMGBSA studies of ethyl-2-amino-4-methyl thiophene-3-carboxylate. *J. Biomol. Struct. Dyn.* **41**, 10411–10429 (2023).
47. Kumar, S. et al. Computational approaches: discovery of GTPase HRas as prospective drug target for 1,3-diazine scaffolds. *BMC Chem.* **13**, 1–13 (2019).
48. Cai, W. et al. Synthesis, evaluation, molecular dynamics simulation and targets identification of novel pyrazole-containing imide derivatives. *J. Biomol. Struct. Dyn.* **39**, 2176–2188 (2021).

49. Mahdavinia, M. et al. Effects of quercetin on bisphenol A-induced mitochondrial toxicity in rat liver. *Iran. J. Basic. Med. Sci.* **22**, 499 (2019).
50. Uzunhisarcikli, M. & Aslanturk, A. Hepatoprotective effects of curcumin and taurine against bisphenol A-induced liver injury in rats. *Environ. Sci. Pollut Res.* **26**, 37242–37253 (2019).
51. Abd-Elnaby, Y. A. et al. Anti-inflammatory and antioxidant effect of Moringa oleifera against bisphenol-A-induced hepatotoxicity. *Egypt. Liver J.l* **12**, 1–8 (2022).
52. Sun, Y. et al. Protective effect of metformin on BPA-induced liver toxicity in rats through upregulation of cystathionine β synthase and cystathionine γ lyase expression. *Sci. Total Environ.* **750**, 141685 (2021).
53. Uzunhisarcikli, M., Aslanturk, A., Kalender, S., Apaydin, F. G. & Bas, H. Mercuric chloride induced hepatotoxic and hematologic changes in rats: the protective effects of sodium selenite and vitamin E. *Toxicol. Ind. Health* **32**, 1651–1662 (2016).
54. Stinghen, A. E., Chillon, J. M., Massy, Z. A. & Boullier, A. Differential effects of indoxyl sulfate and inorganic phosphate in a murine cerebral endothelial cell line (bEnd. 3). *Toxins* **6**, 1742–1760 (2014).
55. Safhi, M. M. et al. Cadmium-induced nephrotoxicity via oxidative stress in male Wistar rats and capsaicin protects its toxicity. *Bull. Environ. Pharmacol. Life Sci.* **5**, 5–11 (2016).
56. Bhattacharjee, A., Basu, A., Ghosh, P., Biswas, J. & Bhattacharya, S. Protective effect of selenium nanoparticle against cyclophosphamide induced hepatotoxicity and genotoxicity in Swiss albino mice. *J. Biomater. Appl.* **29**, 303–317 (2014).
57. Hassan, Z. K. et al. Bisphenol A induces hepatotoxicity through oxidative stress in rat model. *Oxid. Med. Cell. Longev.* **2012**, 194829 (2012).
58. Lin, X. et al. Methyl helicterate protects against CCl4-induced liver injury in rats by inhibiting oxidative stress, NF-κB activation, Fas/FasL pathway and cytochrome P4502E1 level. *Food Chem. Toxicol.* **50**, 3413–3420 (2012).
59. Gur, C., Kandemir, F. M., Caglayan, C. & Satıcı, E. Chemopreventive effects of hesperidin against paclitaxel-induced hepatotoxicity and nephrotoxicity via amendment of Nrf2/HO-1 and caspase-3/Bax/Bcl-2 signaling pathways. *Chemico-Biol. Interact.* **365**, 110073 (2022).
60. Sahin, K. et al. Epigallocatechin-3-gallate activates Nrf2/HO-1 signaling pathway in cisplatin-induced nephrotoxicity in rats. *Life Sci.* **87**, 240–245 (2010).
61. Acaroz, U. et al. Bisphenol-A induced oxidative stress, inflammatory gene expression, and metabolic and histopathological changes in male Wistar albino rats: protective role of boron. *Toxicol. Res.* **8**, 262–269 (2019).
62. Bradham, C. A., Plümpe, J. R., Manns, M. P., Brenner, D. A. & Trautwein, C. I. TNF-induced liver injury. *Am. J. Physiol. -Gastrointest. Liver Physiol.* **275**, G387–G392 (1998).
63. Mirea, A. M., Tack, C. J., Chavakis, T., Joosten, L. A. & Toonen, E. J. IL-1 family cytokine pathways underlying NAFLD: towards new treatment strategies. *Trends Mol. Med.* **24**, 458–471 (2018).
64. Nga, H. T. et al. Interleukin-10 attenuates liver fibrosis exacerbated by thermoneutrality. *Front. Med.* **8**, 672658 (2021).
65. Papa, S., Bubici, C., Zazzeroni, F. & Franzoso, G. Mechanisms of liver disease: cross-talk between the NF-κB and JNK pathways. *Biol. Chem.* **390**, 965–976 (2009).
66. Schmidt-Arras, D. & Rose-John, S. IL-6 pathway in the liver: from physiopathology to therapy. *J. Hepatol.* **64**, 1403–1415 (2016).
67. Zaulet, M. et al. Protective effects of silymarin against bisphenol A-induced hepatotoxicity in mouse liver. *Exp. Ther. Med.* **13**, 821–828 (2017).
68. Facchin, B. M. et al. Evaluation of the anti-inflammatory effect of 1, 4-dihydropyridine derivatives. *Fundam. Clin. Pharmacol.* **38**, 168–182 (2024).
69. Oviedo-Boyso, J., Bravo-Patiño, A. & Baizabal-Aguirre, V. M. Collaborative action of toll-like and NOD-like receptors as modulators of the inflammatory response to pathogenic bacteria. *Mediat. Inflamm.* **2014**, 432785 (2014).
70. He, J. et al. KEAP1/NRF2 axis regulates H2O2-induced apoptosis of pancreatic β-cells. *Gene* **691**, 8–17 (2019).
71. Das, S. et al. Unravelling bisphenol A-induced hepatotoxicity: insights into oxidative stress, inflammation, and energy dysregulation. *Environ. Pollut*. **362**, 124922 (2024).
72. Shalkami, A. G. S. et al. Hepatoprotective effects of phytochemicals berberine and umbelliferone against methotrexate-induced hepatic intoxication: experimental studies and in silico evidence. *Environ. Sci. Pollut Res.* **28**, 67593–67607 (2021).
73. Morteau, O. Prostaglandins and inflammation: the cyclooxygenase controversy. *Inflammation*, 67–81 (2001).
74. Xiao, J. et al. Cyclooxygenase-1 serves a vital hepato-protective function in chemically induced acute liver injury. *Toxicol. Sci.* **143**, 430–440 (2015).
75. Li, H. et al. Toxic effects of bisphenol AF exposure on the reproduction and liver of female marine medaka (Oryzias melastigma). *Animals* **14**, 222 (2024).
76. Xia, W. et al. Early-life exposure to bisphenol a induces liver injury in rats involvement of mitochondria-mediated apoptosis. *PLoS One*. **9**, e90443 (2014).
77. Liu, R. et al. Exposure to bisphenol A caused hepatoxicity and intestinal flora disorder in rats. *Int. J. Mol. Sci.* **23**, 8042 (2022).

Author contributions

The study's conception and design involved the active participation of all the authors. Material preparation, data collection, and analysis were conducted by S.T., M.B., A.A., and Y.D. Pathology studies were performed by S.Y. and İ.B., and in silico studies were carried out by A.H., B.C., and A.S. Both the initial draft and the final scientifically refined version of the manuscript were skillfully crafted by S.T. and M.W. The manuscript underwent critical review and refinement in subsequent iterations, with valuable input from all the authors. The final version of the manuscript was thoroughly examined, assessed, and unanimously approved by all the authors.

Funding

The authors affirm that they did not receive any grants, funds, or other forms of assistance to prepare this manuscript.

Declarations

Competing interests

The authors declare no competing interests.

Ethics statement

This study protocol was approved by the Atatürk University Animal Experiments Local Ethics Committee (HADYEK, Decision No: 2023/87).

Additional information

Correspondence and requests for materials should be addressed to S.T.

Reprints and permissions information is available at www.nature.com/reprints.

Publisher's note Springer Nature remains neutral with regard to jurisdictional claims in published maps and institutional affiliations.

Open Access This article is licensed under a Creative Commons Attribution-NonCommercial-NoDerivatives 4.0 International License, which permits any non-commercial use, sharing, distribution and reproduction in any medium or format, as long as you give appropriate credit to the original author(s) and the source, provide a link to the Creative Commons licence, and indicate if you modified the licensed material. You do not have permission under this licence to share adapted material derived from this article or parts of it. The images or other third party material in this article are included in the article's Creative Commons licence, unless indicated otherwise in a credit line to the material. If material is not included in the article's Creative Commons licence and your intended use is not permitted by statutory regulation or exceeds the permitted use, you will need to obtain permission directly from the copyright holder. To view a copy of this licence, visit http://creativecommons.org/licenses/by-nc-nd/4.0/.

© The Author(s) 2025